AGU PUBLICATIONS

JGR

Journal of Geophysical Research: Atmospheres

RESEARCH ARTICLE
10.1002/2016JD025372

**Key Points:**
- The number of cloud-free hourly observations per day over the Intra-Americas Sea estimated using GOES hourly measurements
- The number of Sun-glint-affected hourly observations per day estimated with the planned GEO-CAPE observation geometry and wind speed
- Provide valuable information for GEO-CAPE mission planning to maximize its value through minimizing the impacts of clouds and Sun glint

**Correspondence to:**
C. Hu,
huc@usf.edu

**Citation:**
Feng, L., C. Hu, B. B. Barnes, A. Mannino, A. K. Heidinger, K. Strabala, and L. T. Iraci (2017), Cloud and Sun-glint statistics derived from GOES and MODIS observations over the Intra-Americas Sea for GEO-CAPE mission planning, *J. Geophys. Res. Atmos.*, *122*, 1725–1745, doi:10.1002/2016JD025372.

Received 16 MAY 2016
Accepted 21 DEC 2016
Accepted article online 22 DEC 2016
Published online 3 FEB 2017



# Cloud and Sun-glint statistics derived from GOES and MODIS observations over the Intra-Americas Sea for GEO-CAPE mission planning

**Lian Feng[1], Chuanmin Hu[1], Brian B. Barnes[1], Antonio Mannino[2], Andrew K. Heidinger[3], Kathleen Strabala[3], and Laura T. Iraci[4]**

[1]College of Marine Science, University of South Florida, Saint Petersburg, Florida, USA, [2]NASA Goddard Space Flight Center, Greenbelt, Maryland, USA, [3]Cooperative Institute for Meteorological Satellite Studies, University of Wisconsin-Madison, Madison, Wisconsin, USA, [4]NASA Ames Research Center, Atmospheric Science Branch, Moffett Field, California, USA

**Abstract** Knowledge of cloud cover, frequency, and duration is not only important to study cloud dynamics, but also critical in determining when and where to take ocean measurements from geostationary orbits such as the Geostationary Coastal and Air Pollution Events (GEO-CAPE) mission due to the challenges in achieving complete hemispheric coverage of coastal oceans, estuaries, and inland waters at hourly frequency. Using GOES hourly measurements at 4 km nadir resolution between 2006 and 2011, the number of cloud-free hourly observations per day ($N_{cf}$) for solar zenith angle $\theta_o < 80°$ was estimated for each 0.1° location of the Intra-Americas Sea. The number of Sun-glint-affected hourly observations per day ($N_{sg}$) was also calculated based on the planned GEO-CAPE observation geometry and realistic wind speed. High-latitude and equatorial oceans showed the lowest $N_{cf}$ (<2.4) in all climatological months, and highest $N_{cf}$ was observed in the Gulf of Mexico (GoM) and Caribbean (>4.5). Different regions showed differences in seasonality of cloud-free conditions and also showed differences in the hour of a day at which the satellite observations would have the maximal cloud-free and glint-free probability ($T_{max}$). Cloud cover from Moderate Resolution Imaging Spectroradiometer (MODIS) 1 km measurements are >10% higher than those from the MODIS 250 m measurements, supporting ocean color missions at subkilometer resolutions to enhance both spatial coverage and temporal frequency. These findings provide valuable information for GEO-CAPE mission planning to maximize its science value through minimizing the impacts of clouds and Sun glint.

## 1. Introduction

Since the proof-of-concept mission Nimbus-7 Coastal Zone Color Scanner, launched by the U.S. National Aeronautics and Space Administration (NASA) in 1978, a number of ocean color missions have been deployed in space by various agencies including NASA, the U.S. National Oceanic and Atmospheric Administration (NOAA), and the European Space Agency, among others [*McClain*, 2009]. The missions include the Sea-viewing Wide Field-of-view Sensor (SeaWiFS; 1997–2010), the Moderate Resolution Imaging Spectroradiometer (MODIS; 1999 to present for Terra and 2002 to present for Aqua), the recent Visible Infrared Imaging Radiometer Suite (VIIRS; 2011 to present), the Medium Resolution Imaging Spectrometer (MERIS; 2002–2012), and the most recent Sentinel-3 Ocean and Land Colour Instrument (OLCI; 2016 to present). These Sun-synchronous polar-orbiting satellite instruments offer near-daily observations of the entire Earth, providing unprecedented information to study the biophysical and biogeochemical properties and processes of the oceans on both global and regional scales.

However, ocean color measurements from these satellite platforms often suffer from several unfavorable measurement conditions, including clouds, Sun glint, cloud adjacent effects, or extreme solar/viewing geometry, leading to a significant reduction in the number of valid observations. Recent estimates by *Feng and Hu* [2016b] showed that the mean daily percentage of valid observations (DPVOs) of surface ocean chlorophyll *a* (Chl *a*) concentrations (in mg $m^{-3}$) from MODIS are generally <20% for most oceans and only <5% for the global mean when 1 km grids are considered. The DPVOs for the normalized Florescence Line Height (nFLH; in $mw^{-2}\,cm^{-2}\,\mu m^{-1}\,sr^{-1}$) data products were even lower, as nFLH is more sensitive than Chl *a* to Sun glint and other contaminations. A similarly low percentage of high-quality ocean color observations was also revealed by *Maritorena et al*. [2010]. This is mostly due to three factors: (1) cloud cover. *King et al*. [2013] reported that the global mean cloudiness over the ocean, based on MODIS estimates, is about 72%;

(2) cloud-adjacent stray light. More than 50% of the cloud-free measurements over the ocean are contaminated by cloud adjacency or cloud-adjacent stray light effects, and they are not used for composition of global level 3 products [*Feng and Hu*, 2016a; *Meister and McClain*, 2010; *Várnai and Marshak*, 2014, 2015], although these effects may eventually be partially corrected [*Feng and Hu*, 2016a]; (3) Sun-glint contamination over the tropical and subtropical oceans [*Feng and Hu*, 2016b]. Due to these nonoptimal observing conditions, for most oceans, there is at most one valid MODIS observation of Chl *a* at a given 1 km grid cell every 5 days, and on average, for the global ocean, there is one valid MODIS observation of Chl *a* at a given 1 km grid cell every 20 days. When multiple pixels are binned to lower-resolution (e.g., 4 km and 9 km) products, the chances of obtaining valid ocean color observations at a given grid cell are higher. However, for coastal oceans and inland waters, subkilometer resolution is often required to observe small-scale features and processes [e.g., *Aurin et al*., 2013], making such an option infeasible.

The low frequency of valid observations from these Sun-synchronous polar-orbiting satellites poses several challenges in addressing key science questions for coastal oceans and inland waters, including documenting diurnal changes in coastal ocean properties, assessing short-term processes, and tracing episodic events. This is because such research requires global ocean coverage in 2–3 days with a spatial resolution of ~1 km, yet after discounting cloud cover and other perturbations the number of valid retrievals is much lower [*Feng and Hu*, 2016b]. In addition, the limited number of valid observations also leads to high uncertainties in data products temporally binned to estimate monthly "mean" values. For example, *Barnes and Hu* [2015] showed that only when both MODIS Aqua (equator overpassing time: ~1:30 P.M.) and SeaWiFS (equator overpassing time: ~12:00 P.M.) provided $>$15 valid observations per month in the open Gulf of Mexico (GoM) could their cross-sensor difference in the monthly mean products reach $<$10% for a given location.

Clearly, more frequent ocean color observations are required. Although this may be partially achieved through multisensor data merging [e.g., *Maritorena et al*., 2010], the ultimate solution is through geostationary satellite observations. As such, the decadal survey of the National Research Council recommended the formulation of a geostationary satellite mission to observe coastal ocean and air quality [*NRC*, 2007]. In response to this recommendation, NASA has been developing the next-generation ocean color mission, namely, the Geostationary Coastal and Air Pollution Events (GEO-CAPE) [*Fishman et al*., 2012], with mission specifications and planning defined in the past few years. NASA has supported GEO-CAPE preformulation activities from 2008 to the present that encompass engineering studies and scientific research relevant for mission risk reduction. Atmospheric and ocean science working groups (SWGs) were established to define the high-priority mission science questions and associate them with specific measurement and instrument requirements [*Fishman et al*., 2012]. Engineering studies have demonstrated the technological readiness and refined the costs of the mission concept and notional satellite instruments. The science studies have constrained and justified the measurement and instrument requirements such as spatial and temporal resolutions. All these activities have been summarized in a detailed whitepaper available online (http://geo-cape.larc.nasa.gov/pdf/GEO-CAPE_2009-2015_SummativeWhitePaper.pdf). GEO-CAPE and four other missions were originally envisioned with notional launch dates of 2013–2016 ("Tier 2"). Due to budget and other constraints, none of the Tier 2 missions have yet advanced to mission formulation with established launch dates.

A geostationary sensor could obtain multiple observations per day at any given location within its field of view (FOV). With 8-hourly measurements per day, the proof-of-concept Geostationary Ocean Color Imager (2010 to present) has already demonstrated the increased value of high temporal observations over the low-Earth orbiting sensors in capturing short-term changes of water turbidity, red tides, floating algae, etc., over coastal waters around South Korea, East China Sea, and the Yellow Sea [*Choi et al*., 2012; *He et al*., 2013; *Lou and Hu*, 2014; *Son et al*., 2012]. However, to maximize the capacity of GEO-CAPE in addressing the various science needs [*Fishman et al*., 2012], one practical consideration is when and where to take measurements. This is because in practice, and particularly for the high-resolution (250 to 375 m) GEO-CAPE ocean color mission, it is impossible to measure *all* targets within the satellite's potential FOV on an hourly basis due to sensor technical and cost limitations, leading to competing demands to measure different regions [*Fishman et al*., 2012]. In contrast to geostationary weather satellites (such as the instruments aboard the current series of Geostationary Operational Environmental Satellite (GOES) system), which can scan most of the Earth disk 2 or more times per hour, sensor concepts capable of meeting or exceeding the minimum GEO-CAPE ocean color accuracy requirements have much lower scan rates (area per unit time), ranging from

~25,000 to over 100,000 $km^2$ $min^{-1}$. This scan rate places an upper limit on the area that can be imaged and at a given temporal frequency. The GEO-CAPE SWG recommended a minimum daytime target mode acquisition frequency of hourly observations (30 min goal) for imaging hazards or other critical events and a 2 h frequency (1 h goal) for survey mode scans of U.S. continental coastal and inland waters. The discrepancy in observation frequency between weather and ocean color sensors is due primarily to two factors (ignoring instrument design differences), the signal-to-noise ratio and spatial resolution, both of which are higher for ocean color sensors. If a GEO-CAPE sensor can bypass scanning heavily clouded scenes based on a priori knowledge of cloud cover at the time of sensor scanning and historical cloud cover statistics, it allows for optimization of the available scan time to concentrate on likely cloud-free or partially cloudy scenes. This capability affords a significant measure of efficiency and increases the frequency and area that can be scanned within a given day. Recent and ongoing work involves evaluation of the feasibility of using intelligent cloud avoidance strategies with notional instrument concepts to explore various scenarios incorporating actual cloud forecast data for specific targets.

Thus, it is desirable to determine the optimal observation time window for a given region, essentially identifying the best season (or month) and best observation time during the day to acquire observations for a certain region. While this can also be driven by a particular science question (e.g., *Karenia brevis* blooms on the west Florida shelf typically occur from summer to fall), knowledge of the optimal measurement conditions, such as probability of cloud cover and Sun glint, can help implement an optimal measurement plan.

Although cloud cover has been estimated from MODIS cloud mask products [*Ackerman et al*., 2008; *King et al*., 2013], such statistics are based primarily on daily snapshot measurements around solar noon (except for the polar regions) and are thus not sufficient to provide statistics for the entire day, as required for geostationary satellites. GOES, on the other hand, has provided the most frequent cloud observations over the continental United States, the Pacific and Atlantic Oceans, Central and South America, and southern Canada [*Lombardi and Hanson*, 2005] since 1974. As such, the cloud masks provided by GOES are the most suitable data to determine the cloud-free time window for the planed FOV of GEO-CAPE. The goal of this study is therefore to demonstrate how geostationary missions such as GEO-CAPE with their capability to collect data at any time during the day can provide greater ocean color coverage than Sun-synchronous ocean color sensors (SeaWiFS, MODIS, MERIS, VIIRS, OLCI, and the future PACE (Plankton, Aerosols, Clouds, ocean Ecosystems) mission), with the following specific objectives:

1. apply GOES observations to determine diurnal to seasonal variability in cloud cover to demonstrate how geostationary orbit could improve clear-sky coverage of ocean color observations compared to Sun-synchronous low-Earth orbit,
2. determine how Sun glint constrains diurnal observations of ocean color from geostationary orbit,
3. evaluate to what extent higher satellite sensor spatial resolution affects the extent of cloud-free areas by comparing cloud cover statistics derived from measurements obtained at different spatial resolutions, and
4. discuss the implications of cloud and glint distributions for future GEO ocean mission planning such as GEO-CAPE.

Note that although the focus of this study is for ocean measurements, the cloud statistics over land are also estimated and presented for reference purposes.

## 2. Data Sources

Three data sets are used in this study to estimate cloud-free probability (or cloud statistics) for the study region: (1) GOES cloud masks between 2006 and 2011 at 4 km nadir resolution but resampled to 0.1°; (2) concurrent cloud fraction products from MODIS Aqua (MYD08) for daytime observations at 1°, derived from measurements at 1 km nadir resolution; and (3) MODIS cloud masks from the MOD35 (Terra) and MYD35 (Aqua) data products at 1 km and 250 m nadir resolutions in the years of 2005, 2008, 2011, and 2014.

### 2.1. GOES Data

The GOES observations provide five spectral channels with central wavelengths of approximately 0.65, 3.9, 6.7, 11.0, and 13.3 μm. The nadir spatial resolution of the data used here is 4 km, where 1 km visible bands were resampled into 4 km to match the spatial resolution of the infrared bands. However, the data analyzed in this study were resampled to a 0.1° resolution as described in *Heidinger et al*. [2014]. The GOES sensors

generate data over multiple domains with differing temporal resolutions. This study uses the Northern Hemisphere extended domains observed at 15 min after the start of each hour from the GOES 12 and GOES 13 satellites, which were located at 75°W. Note that the GOES 13 satellite replaced GOES 12 satellite on 14 April 2010, while the two satellites share very similar cloud detection capability (http://www.nasa.gov/mission_pages/goes-n/media/goes-east.html). The GOES data were processed through the NOAA/National Environmental Satellite, Data, and Information Service Clouds from Advanced Very High Resolution Radiometer Extended (CLAVR-x) processing system, which utilizes the community-accepted NOAA Enterprise Cloud Algorithms (ECAs) [*Heidinger et al*., 2012]. As the name implies, these algorithms are applied to all of the sensors supported by NOAA, including GOES.

The NOAA ECA is described in *Heidinger et al*. [2012]. It uses a naïve Bayesian formulation to combine the results of multiple spectral and spatial cloud detection classifiers into a single value of the probability that a pixel is cloudy. The cloud detection scheme also generates a four-tier probability cloud mask with the values of 0 = confidently clear, 1 = probably clear, 2 = probably cloudy, and 3 = confidently cloudy. The four-level mask is derived solely from the cloud probability values, with the cloud probability value that separates confidently and probably clear being 0.1. One of the advantages of this technique is that the most suitable threshold can be selected according to the needs of any specific applications. We used the value of 0 (e.g., confidently clear) to conduct the cloud-free statistics in this study.

In addition to the cloud mask, this study also used the solar geometry information from CLAVR-x. CLAVR-x also includes the surface wind speed and direction in its output, which is obtained from the Climate Forecast System Reanalysis (CFSR) data. CFSR data have a resolution of 0.5° and temporal resolution of 6 h. A linear interpolation in space and time was used to generate the CFSR data for each GOES pixel. The solar geometry and wind speed were used to estimate the corresponding Sun-glint reflectance for the planned GEO-CAPE viewing geometry.

### 2.2. MODIS Data

To evaluate the impact of pixel resolution on cloud statistics, level-3 1° × 1° daytime cloud fraction products were obtained from the Geospatial Interactive Online Visualization And aNalysis Infrastructure of the Goddard Earth Sciences Data and Information Services Center [*Acker and Leptoukh*, 2007]. Cloud fraction was first derived from the MODIS/Aqua cloud mask products (MYD35) at 1 km nadir resolution [*Ackerman et al*., 1998], which is defined as the number of cloudy pixels divided by the total number of measured pixels in each gridded cell [*Platnick et al*., 2003], and the level 3 monthly cloud fraction ($C_f$) data were mapped to a 1° × 1° grid on an equal-angle projection.

In order to derive 250 m and 1 km resolution cloud fractions, MODIS level 1B data were locally processed using the official MOD35 cloud mask algorithm, where a series of individual spectral tests were employed to determine a final four-category confidence of clear sky for a given field of view (FOV) [*Ackerman et al*., 1998]. In practice, the collection 6 NASA MODIS MODI35 cloud mask baseline software was ported from the operational MODIS atmosphere group-processing environment for stand-alone execution as part of the International MODIS/AIR Processing Package (IMAPP) [*Huang et al*., 2004]. Designed for MODIS global direct broadcast users, it can be used to process any standard MODIS L1B-calibrated, geolocated data set on standard Linux operating systems.

Throughout this manuscript, the terms cloud amount, cloud cover, cloud frequency, etc., are used to describe the quantity retrieved from the GOES and MODIS measurements and the corresponding algorithms. These terms are shorthand for occurrence frequency of cloud-contaminated pixels. In other words, cloud masking/detection algorithms do not provide a measure of cloud amount in a pixel but rather provide an indication of the likelihood of a pixel's instantaneous FOV being obstructed by a cloud element.

## 3. Methods

### 3.1. Cloud Statistics

The number of discrete cloud-free hourly observations in a day ($N_{cf}$) is one of the most important parameters of this study, which was estimated as the summation of the number of cloud-free GOES observations during a day when solar angle $\theta_o$ was $<80°$. Data with $\theta_o > 80°$ were excluded because the ocean color signal for such targets would be too small and overwhelmed by sky Fresnel reflectance [*Gordon*, 1997; *Kirk*, 1994]. The

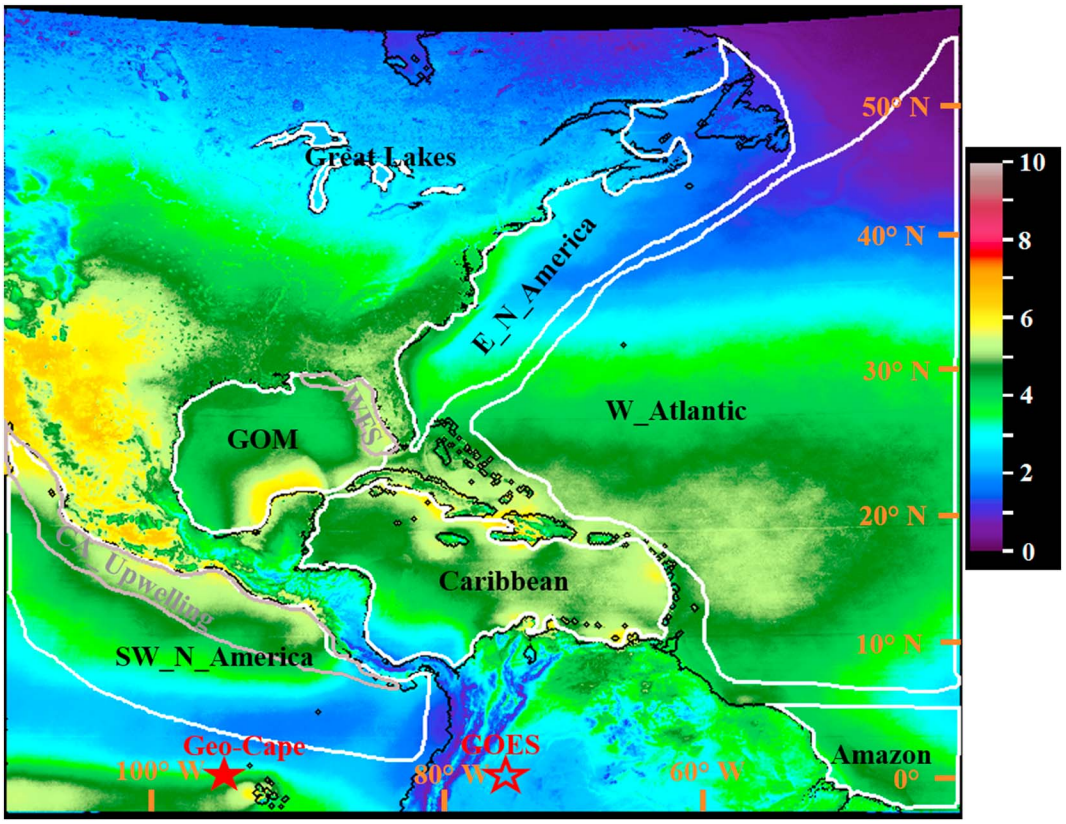


**Figure 1.** Map of the GOES observation area (rather than GEO-CAPE) used in this study. The color shows the mean number of cloud-free hourly observations during a day ($N_{cf}$) for Sun elevation $> 10°$ (i.e., solar zenith angle $\theta_o < 80°$), based on GOES cloud cover data (4 km resolution but resampled to 0.1°) between 2006 and 2011 and Sun angle calculation for each location. The oceans and lakes are partitioned into subregions (white and grey lines) to facilitate calculation of regional statistics. The locations of GOES (75°W over the equator) and GEO-CAPE satellite (94°W as currently being planned) are annotated.

integrated daily cloud-free probability ($P_{cf}$) was also estimated and was used to assess the potential capability of the geostationary satellite in obtaining at least one cloud-free observation in any given day. If there was at least one cloud-free observation in a day, the $P_{cf}$ is set as 100%. Then, the monthly mean $N_{cf}$ (or $P_{cf}$) was calculated as the integration of $N_{cf}$ (or $P_{cf}$) in that month normalized by the number of days. Note that in this analysis, whether an observation was over clouds was determined purely from the cloud detection algorithms for GOES and MODIS, where absorption by aerosols and gases were not considered.

### 3.2. Sun-Glint Statistics

The Sun-glint strength, defined as the normalized Sun-glint reflectance, or $L_{gn}$ (in $sr^{-1}$), was estimated as a function of wind speed (to estimate the surface roughness) and solar/viewing geometry [*Cox and Munk*, 1954; *Wang and Bailey*, 2001; *Zhang and Wang*, 2010]. For each GOES hourly observation, $L_{gn}$ was estimated using the time of the observation, windspeed of the observation (obtained from the CFSR), and the planned observational geometry of GEO-CAPE. The proposed orbital location (for GEO-CAPE 94°W; annotated in Figure 1) was used to calculate the view zenith and azimuth angles for each target, and the GOES observation time was used to estimate the solar zenith and azimuth angles [*Richharia*, 2014]. Following the same convention that is used as the NASA standard quality control flag in composing global chlorophyll *a* data products, "high-glint" observations with $L_{gn} \geq 0.005\ sr^{-1}$ were considered as Sun-glint-affected data [*Wang and Bailey*, 2001]. Similar to calculating cloud statistics, the number of Sun-glint-affected hourly observations within a day ($N_{sg}$) and the monthly mean $N_{sg}$ were estimated. With the cloud and Sun-glint coverage, cloud-free and glint-free pixels can be identified for each hourly geostationary satellite image, and the numbers of cloud-free and glint-free observations in a day (or $N_{cg}$) were calculated, as were the corresponding monthly

data. Note that although wind conditions from cloud fields may have a secondary effect on Sun-glint calculations, such an effect was not considered in this study.

With the hourly cloud-free and glint-free observations between 2006 and 2011, the time of a day (or Greenwich Mean Time (GMT) hour, specifically) that has the maximal cloud-free and glint-free probability (or $T_{max}$) for a location can be determined. As $T_{max}$ may change with season due to the variability of cloud cover and Sun glint, $T_{max}$ was obtained for each climatological month (2006–2011). Additionally, the mode of the histogram of the optimal hour (for cloud-free probability) from all pixels within the predefined regions was estimated for each climatological month, representing the mean condition for that region.

### 3.3. Comparison Between Cloud Statistics for Different Spatial Resolutions

There are two comparisons in the study. The first compares GOES 4 km cloud statistics with MODIS 1 km cloud statistics, and the second compares MODIS 1 km cloud statistics with MODIS 250 m cloud statistics.

For each 1° region of the level 3 MODIS monthly cloud fraction data, the noncloud fraction was calculated as $1 - C_f$, which can also be interpreted as noncloud probability. The GOES cloud mask data closest in time during each day to the MODIS/Aqua observation (e.g., 13:15 local time) were used to generate similar monthly noncloud fraction products as MODIS/Aqua following the methods of *Platnick et al*. [2003].

Daily MODIS (Aqua and Terra) passes covering the GoM region (18–31°N, 98–79°W) collected during the years 2005, 2008, 2011, and 2014 were downloaded at level 1A from the NASA Ocean Biology Processing Group archives (http://oceancolor.gsfc.nasa.gov). These data were processed to level 1B using SeaDAS (version 7.2) with default processing parameters. L1B data were subsequently processed using IMAPP (version 3.1; corresponding to collection 6 [*Huang et al*., 2004]) and mapped to an equidistant cylindrical projection (with the GoM geographical bounds specified above) at 1 km spatial resolution. From this, the 1 km MOD35 cloud mask was created as pixels where the MOD35 algorithm ran without failure (bit 0), classified the target as water (value 0 in bits 6–7), and identified the target as "probably cloudy" or "confident cloudy" (values 0 and 1 in bits 1–2). The projected MOD35 data were also used to create 250 m (QKM) cloud masks, using quality-assurance bits 25–40 (to identify algorithm failure) and cloud mask bits 32–47 (for determination of cloud presence/absence). Monthly (and yearly) cloud cover over water for the 1 km and QKM cloud masks was determined as the total number of cloudy pixels divided by the total number of observed pixels. This latter classification was determined at 1 km spatial resolution and multiplied by 16 to calculate the denominator for QKM cloud cover percentages.

## 4. Results

### 4.1. Cloud and Sun-Glint Statistics From GOES Measurements and GEO-CAPE Geometry

The number of cloud-free hourly observations in a day ($N_{cf}$) during the period of 2006–2011 is shown as the base map in Figure 1. For the entire study area, the eastern Caribbean and southern GoM show the highest $N_{cf}$, with 5–7 cloud-free hourly observations during an average day for Sun elevation $>10°$. Certain ocean regions also show relatively high daytime cloud-free periods (yellowish in Figure 1), such as the California upwelling region off the southwest coast of the North America, as well as the western Atlantic. In contrast, the higher-latitude regions ($>35°$N for the open ocean and $>40°$N for land and ocean) are more influenced by clouds, where the mean $N_{cf}$ values are generally $<3$. In addition, low $N_{cf}$ values are also observed in the equatorial eastern Pacific Ocean.

The monthly climatological $N_{cf}$ distributions are shown in Figure 2, where significant intraannual variability is revealed across the panels. For example, while a large area of the southwest coast of North America shows high $N_{cf}$ from November to April, warmer months from May to October tend to have more cloud coverage. In contrast, a higher cloud-free probability occurs in late spring and summer months in the GoM than in the other seasons. Similar seasonality is also observed for the western Atlantic Ocean. On the other hand, clouds are frequently present in the equatorial regions through most of the year, except for certain months over ocean waters close the Amazon delta.

Statistics of $N_{cf}$ for the predefined regions are presented in Table 1. The two regions at relatively high latitudes (eastern coast of the North America and the Great Lakes) show the lowest $N_{cf}$ among these areas, with mean hourly cloud-free observations of $<2.4$ and even $<1$ for some winter months. The GoM and

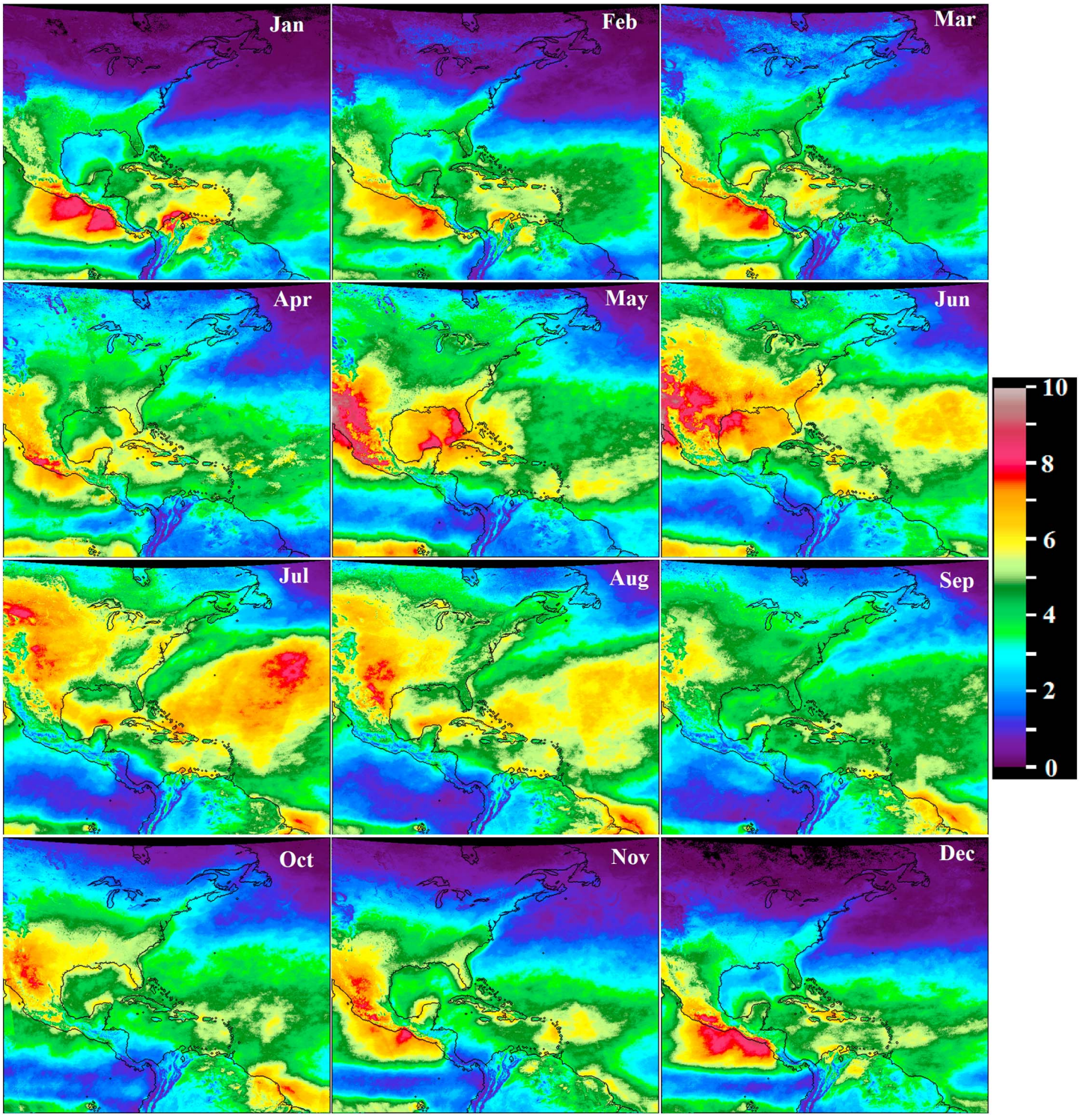


**Figure 2.** Mean number of cloud-free hourly observations per day ($N_{cf}$) for each climatological month (2006–2011) for solar angle $\theta_o < 80°$. Statistics for the predefined subregions are presented in Table 1.

Caribbean oceans show the higher cloud-free probability, with an annual mean $N_{cf}$ of >4.5 for the two regions. The cloud-free probability is even higher for the West Florida Shelf (WFS) of the GoM. Additionally, while the cloud coverage is relatively stable throughout the year in the Caribbean, in the GoM more cloud-free opportunities occur in warm months ($N_{cf}$ >6 and even >7 in WFS in May) than in cold months (<3 in

**Table 1.** Mean Number of Cloud-Free Hourly Observations Within a Day ($\theta_o < 80°$) for Each Climatological Month Between 2006 and 1010, Based on GOES Observations at 4 km Resolution[a]

| | E_Atlantic | Amazon | Caribbean | E_N_America | G_Lakes | SW_N_America | CA_Upwelling | GoM | WFS |
|---|---|---|---|---|---|---|---|---|---|
| Jan | 2.8 (0.3) | 2.7 (0.6) | 5.3 (0.6) | 0.8 (0.1) | 0.3 (0.1) | 5.4 (0.4) | 6.7 (0.4) | 3 (0.6) | 3.6 (0.7) |
| Feb | 2.6 (0.8) | 2 (0.8) | 5 (1.7) | 0.9 (0.4) | 0.6 (0.3) | 5.2 (2.2) | 6.3 (2.4) | 3.2 (1.7) | 3.8 (1.9) |
| Mar | 2.6 (1.2) | 2.3 (1.2) | 4.9 (2.3) | 1.7 (0.8) | 1.8 (0.9) | 5.4 (2.6) | 6.5 (3) | 4.1 (1.9) | 4.8 (2.3) |
| Apr | 3.1 (1.4) | 1.8 (1) | 4.8 (2.3) | 2.5 (1.1) | 2.3 (1.1) | 4.4 (2.1) | 5.6 (2.6) | 5 (2.4) | 5.8 (2.7) |
| May | 3.9 (0.3) | 2.6 (0.5) | 4.8 (0.4) | 3.4 (0.5) | 3.3 (0.8) | 3.2 (0.4) | 4.6 (0.4) | 6.9 (0.8) | 7.5 (0.8) |
| Jun | 4.4 (0.3) | 3.8 (0.7) | 4.4 (0.6) | 3.7 (0.5) | 4.2 (0.8) | 2.5 (0.3) | 3.7 (0.4) | 6.7 (0.6) | 6.7 (0.7) |
| Jul | 5.5 (0.3) | 5.3 (0.6) | 4.6 (0.9) | 3.7 (0.3) | 5.2 (0.7) | 1.9 (0.5) | 2.8 (0.7) | 5.5 (0.7) | 5.1 (0.5) |
| Aug | 4.9 (0.7) | 5.7 (0.9) | 4.7 (0.9) | 3.7 (0.8) | 5.2 (0.9) | 1.8 (0.5) | 2.6 (0.7) | 5.4 (0.2) | 4.9 (1) |
| Sep | 3.9 (1.4) | 5.8 (2) | 4.1 (1.5) | 2.9 (0.9) | 3.1 (1.3) | 1.9 (0.9) | 2.5 (1.2) | 4.2 (1.7) | 4.4 (1.8) |
| Oct | 2.8 (1.4) | 4.9 (2.5) | 3.2 (1.8) | 2 (1) | 1.4 (1.1) | 2.5 (1.4) | 3.5 (2) | 4 (2.2) | 4.5 (2.5) |
| Nov | 2.9 (0.2) | 4.7 (0.4) | 4.1 (0.8) | 1.4 (0.2) | 0.8 (0.3) | 4.4 (0.4) | 6.2 (0.5) | 4.2 (0.9) | 4.9 (1.1) |
| Dec | 2.2 (1.1) | 3 (1.7) | 4 (2.1) | 0.7 (0.4) | 0.3 (0.2) | 4.2 (2.1) | 5.6 (2.8) | 2.5 (1.4) | 2.9 (1.8) |
| Mean | 3.5 (0.8) | 3.7 (1.1) | 4.5 (1.3) | 2.3 (0.6) | 2.4 (0.7) | 3.6 (1.1) | 4.7 (1.4) | 4.6 (1.3) | 4.9 (1.5) |

[a]Numbers in the parentheses are standard deviations. Spatial distributions are presented in Figure 2.

December). Similar seasonal patterns are also found in the eastern Atlantic and the Amazon plume areas, where $N_{cf}$ is >5 in boreal summer but drops to ~2 in winter. In contrast, while $N_{cf}$ is >5 during boreal winter months along the southwest coast of North America, $N_{cf}$ decreases to <2 in warmer months. The California upwelling region shares seasonal patterns similar to the southwest coast of North America but with higher probability of cloud-free conditions ($N_{cf}$ ~4–6 in autumn-winter-spring and ~2–3 in warmer months).

A 6 year mean daily cloud-free probability, $P_{cf}$, for each climatological month between 2006 and 2011 was calculated and is shown in Figure 3, with numeric values (including standard derivations) for the predefined regions shown in Table 2. The values can be interpreted as the probability of obtaining at least one cloud-free observation during a day in that month for solar angle $\theta_o < 80°$. Other than some high-latitude regions and the equatorial oceans, most of the study regions have a probability of >50% in obtaining daily cloud-free images with hourly observational frequency in any climatological month. While the mean $P_{cf}$ for the eastern coast of North America (particularly in the northeast) and the Great Lakes is <50% on average and even <25% for certain months, mean $P_{cf}$ is >62.5% for other predefined regions. Additionally, seasonal variability is also found in most regions, where the spatial patterns are generally the same as in the climatological $N_{cf}$.

The mean daily number of hourly observations affected by Sun glint, $N_{sg}$, during each climatological month of 2006–2011 was estimated and is illustrated in Figure 4, while the statistics for different regions are tabulated in Table 3. Significant spatial and temporal gradients are observed. As expected, boreal summer months are more likely to be influenced by Sun glint than winter months. Between April and September, a large portion of the study region shows $N_{sg}$ of 3–4 (green color in Figure 4), especially for the northeastern coast of South America (including the Caribbean Sea) and the equatorial oceans. In contrast, the Sun-glint-affected areas are restricted only to the equatorial oceans from October to February. Statically, the oceans close to the Amazon delta show the highest probability of Sun-glint presence, with a 12 month mean climatological $N_{sg}$ of 2, suggesting that two daytime hourly observations would be contaminated by Sun glint in this region in an average day. Other areas affected by Sun glint include the eastern Atlantic Ocean, Caribbean Sea, southwestern coast of the North America, and the GoM, with mean $N_{sg}$ reaching to 1 (or close to 1). However, the California upwelling region and WFS show limited influence with mean $N_{sg}$ of 0.2 and 0.1, respectively. The two high-latitude regions (eastern coast of the North America and the Great Lakes) are not affected by Sun glint due to their relatively low solar angles and large viewing angles.

Daily cloud-free and glint-free hourly observations ($N_{cg}$) during each climatological month of 2006–2011 were estimated and presented in Figure 5. The values are similar to the $N_{cf}$ in Figure 3, especially for high-latitude regions. Major difference is found in the equatorial regions from the northwest to South America. In these regions, $N_{cf}$ is generally ≥4 but $N_{cg}$ is <4 due to severe Sun glint. Differences are also observed in the Amazon outflow region, Caribbean Sea, and GoM, especially during some boreal summer months.

The GMT hour at which the satellite observations would have the maximal cloud-free and glint-free probability ($T_{max}$) is color coded in Figure 6, where each panel represents a climatological month. Significant

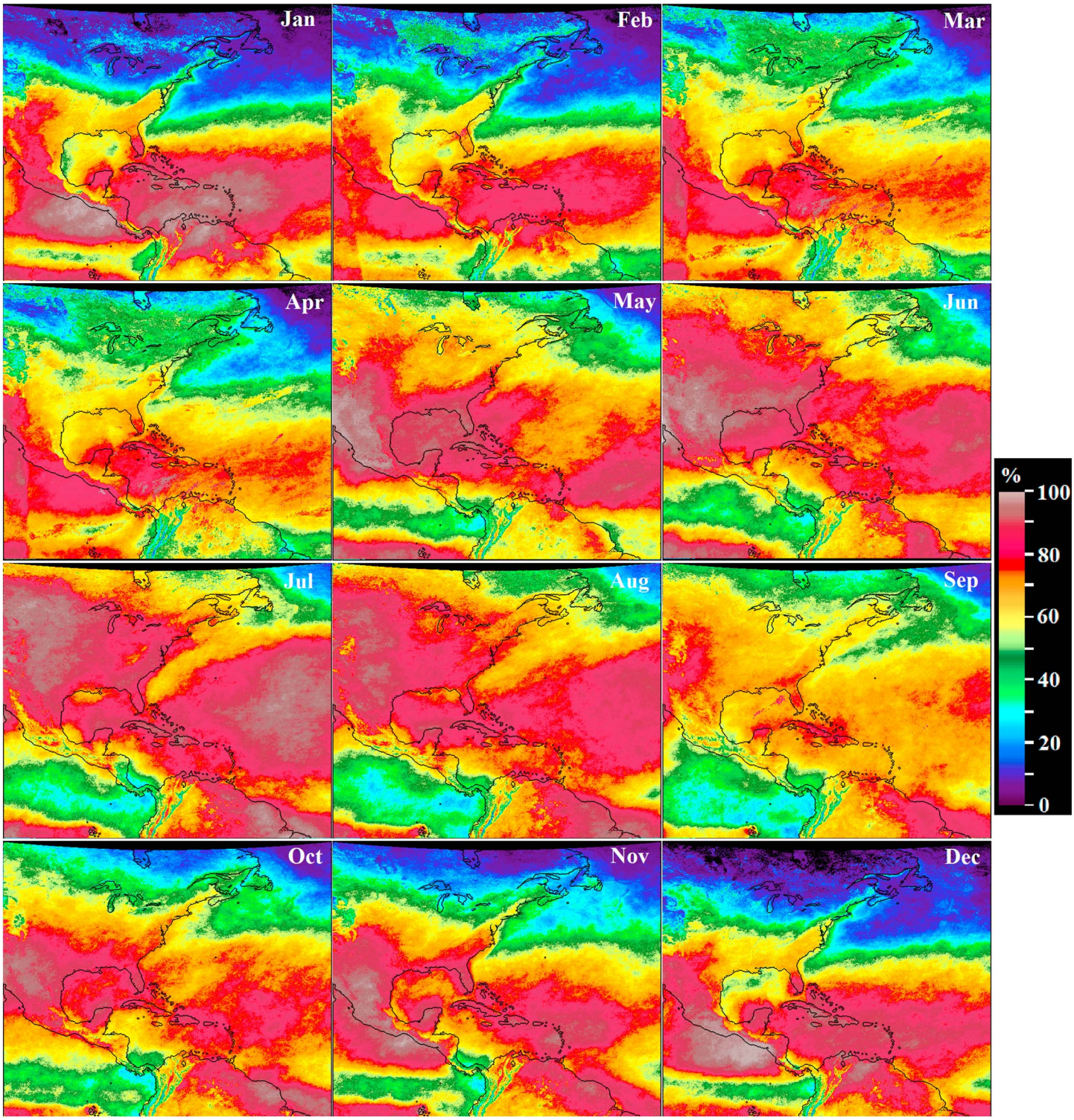


**Figure 3.** Mean-integrated daily cloud-free probability ($P_{cf}$) within a day for each climatological month (2006–2011) for solar angle $\theta_o < 80°$. A value of 70% means that for a given day there is a 70% chance of getting at least one cloud-free observation from all hourly observations. Statistics for the predefined subregions are presented in Table 2.

**Table 2.** Mean-Integrated Daily Cloud-Free Probability (%) Within a Day in Each Climatological Month (2006–2010) for Solar Angle $\theta_o < 80°$[a]

| | E_Atlantic | Amazon | Caribbean | E_N_America | G_Lakes | SW_N_America | CA_Upwelling | GoM | WFS |
|---|---|---|---|---|---|---|---|---|---|
| Jan | 60.5 (4.4) | 59.1 (9.1) | 89 (4.5) | 24.5 (3.6) | 13.7 (3.1) | 82.1 (3.1) | 90 (3.7) | 62.1 (10.3) | 69.1 (8.7) |
| Feb | 54.4 (17.2) | 44.3 (17.1) | 79.6 (27) | 24.8 (10) | 20.1 (7.9) | 75.1 (25.6) | 80.5 (27.1) | 60.5 (27.9) | 64.3 (27.4) |
| Mar | 53.1 (24.7) | 45.6 (23.3) | 75.4 (35.4) | 36.5 (16.5) | 40.6 (19.4) | 75.9 (29.8) | 81.9 (31.5) | 66.6 (31.5) | 69.9 (33.1) |
| Apr | 57 (26.4) | 40.4 (19.8) | 71.3 (33.6) | 45.4 (20.8) | 45.9 (21.6) | 67.8 (25.8) | 77.9 (27.5) | 72.3 (34.4) | 74.3 (34.9) |
| May | 68.1 (3) | 55.2 (7) | 75 (4.1) | 59.1 (4.5) | 59.9 (6.9) | 58.6 (4.2) | 71.7 (3.2) | 89 (4.9) | 89.8 (5.1) |
| Jun | 71.7 (2.7) | 69.1 (7) | 70 (5.9) | 63.3 (5.5) | 70.8 (6.6) | 51.2 (5.4) | 62.5 (5.8) | 85.4 (5) | 86 (3) |
| Jul | 81.5 (2.7) | 83.3 (4) | 73.1 (8.8) | 65.8 (3.3) | 80.8 (5.2) | 44.4 (8.4) | 57 (10) | 79.5 (4.6) | 79.1 (4.8) |
| Aug | 74.7 (10.6) | 82.7 (11.2) | 71.9 (11.7) | 64.7 (11.1) | 77.6 (11.3) | 41.7 (8.6) | 53.5 (9.6) | 80.1 (8.3) | 76.1 (12.4) |
| Sep | 64.4 (22.7) | 78.9 (27.8) | 65.5 (23.1) | 55.5 (17.9) | 55.8 (19.6) | 41.3 (16.3) | 50 (19.9) | 67.2 (26.5) | 69.9 (28.2) |
| Oct | 54.5 (26.9) | 71.8 (35.3) | 56.9 (29) | 43.1 (21.7) | 34 (20.7) | 45.8 (23.3) | 55 (28.7) | 66.5 (33.4) | 68.5 (34.5) |
| Nov | 61.2 (3.5) | 80 (3.3) | 73.2 (7.7) | 37.9 (4.2) | 24.8 (6.7) | 71.9 (4.1) | 87.6 (4.9) | 76.9 (10.9) | 81.7 (10) |
| Dec | 49.4 (24.2) | 57.9 (29.6) | 70.3 (35.1) | 21.1 (11.4) | 10.9 (6.1) | 65.5 (32.2) | 75.8 (37.2) | 52.7 (28.1) | 56.1 (30.8) |
| Mean | 62.5 (10.5) | 64 (10.9) | 72.6 (12.8) | 45.1 (6.9) | 44.6 (7) | 60.1 (11.1) | 70.3 (12.5) | 71.6 (12.3) | 73.8 (13) |

[a]A value of 70% means that on average, for a given day in that month, there is 70% probability to have at least one cloud-free measurement from all hourly measurements. Numbers in the parentheses are standard deviations. Spatial distributions are presented in Figure 3.

variability is found in different locations and seasons. The most prominent seasonality occurs in the Caribbean, where the $T_{max}$ ranges between 13 August–November and 20 February–June. Other noticeable seasonality occurs in regions including the eastern coast of North America ($T_{max}$ = 14–22), the southwestern coast of North America ($T_{max}$ = 15–20), and the GoM ($T_{max}$ = 15–20). $T_{max}$ for the California upwelling region is higher (i.e., later in the day) than that of the southwestern coast of North America, ranging from 19 November to 22 May–August. $T_{max}$ for the WFS is also different from other parts of the GoM, with less apparent seasonality. The western Atlantic Ocean has a mean $T_{max}$ of 13–14 for most of the year (Table 4), while $T_{max}$ for a large portion of this region is 1–2 h higher in boreal summer months than in other months. Relatively stable conditions are also found for the Great Lakes ($T_{max}$ = 17–20) and the ocean region close to Amazon delta ($T_{max}$ = 14–15).

### 4.2. Cloud Statistics of Different Resolutions

Spatial resolution of satellite measurements can affect the cloud cover estimates, as can be imagined by taking the following extreme case for example: if the entire global ocean is treated as one pixel then this pixel is always a cloudy pixel because 70% of the global ocean is cloudy [*King et al.*, 2013]. Thus, finer-resolution measurements would lead to less cloud cover. Here the resolution-induced uncertainties in cloud statistics are evaluated through comparison between concurrent GOES and MODIS 1 km cloud statistics and between MODIS 1 km and 250 m (QKM) cloud statistics.

First, monthly cloud-free probabilities estimated from GOES and MODIS/Aqua are compared. MODIS data are collected at 13:30 local time over the equator, while the corresponding GOES data are collected at 13:15 local time. The spatial distributions of $P_{cf}$ from these two measurements for two typical months are shown in Figure 7. The GOES-derived cloud-free probabilities appear very similar to those of MODIS/Aqua, especially for the low-latitude regions. For example, high $P_{cf}$ values are observed over the GoM and western portions of the Atlantic and the western areas of North America from both measurements in June. Meanwhile high cloud coverage is shown through almost the entire Pacific region west of Central America. In contrast, in December both measurements show very high cloud-free probability in the southwest coast of the North America. The agreement between these two sets of independent observations is further proven in the scatterplots in Figure 8 for ocean observations only, where the relationships between the two are statistically significant and most data points are generally aligned around the 1:1 line, with median ratios between the two observations (GOES versus Aqua) being 1.05 and 1.03 for June and December, respectively. Other months show similarly consistent cloud coverage between GOES and MODIS/Aqua observations. However, differences in $P_{cf}$ can also be observed between MODIS and GOES observations. There may be several reasons explaining the differences. First, the spatial resolution of GOES is lower than MODIS, especially for high-latitude regions as GOES pixel size systematically increases with viewing angle (see GOES pixel size contours in Figures 7a and 7d). Second, the lack of spectral information on the GOES imager (compared to MODIS) makes it difficult to discriminate clouds. Third, cloud detection algorithms, namely, CLAVR-x for GOES and MOD35 for MODIS, are also different. These potential reasons may also explain the relatively large differences

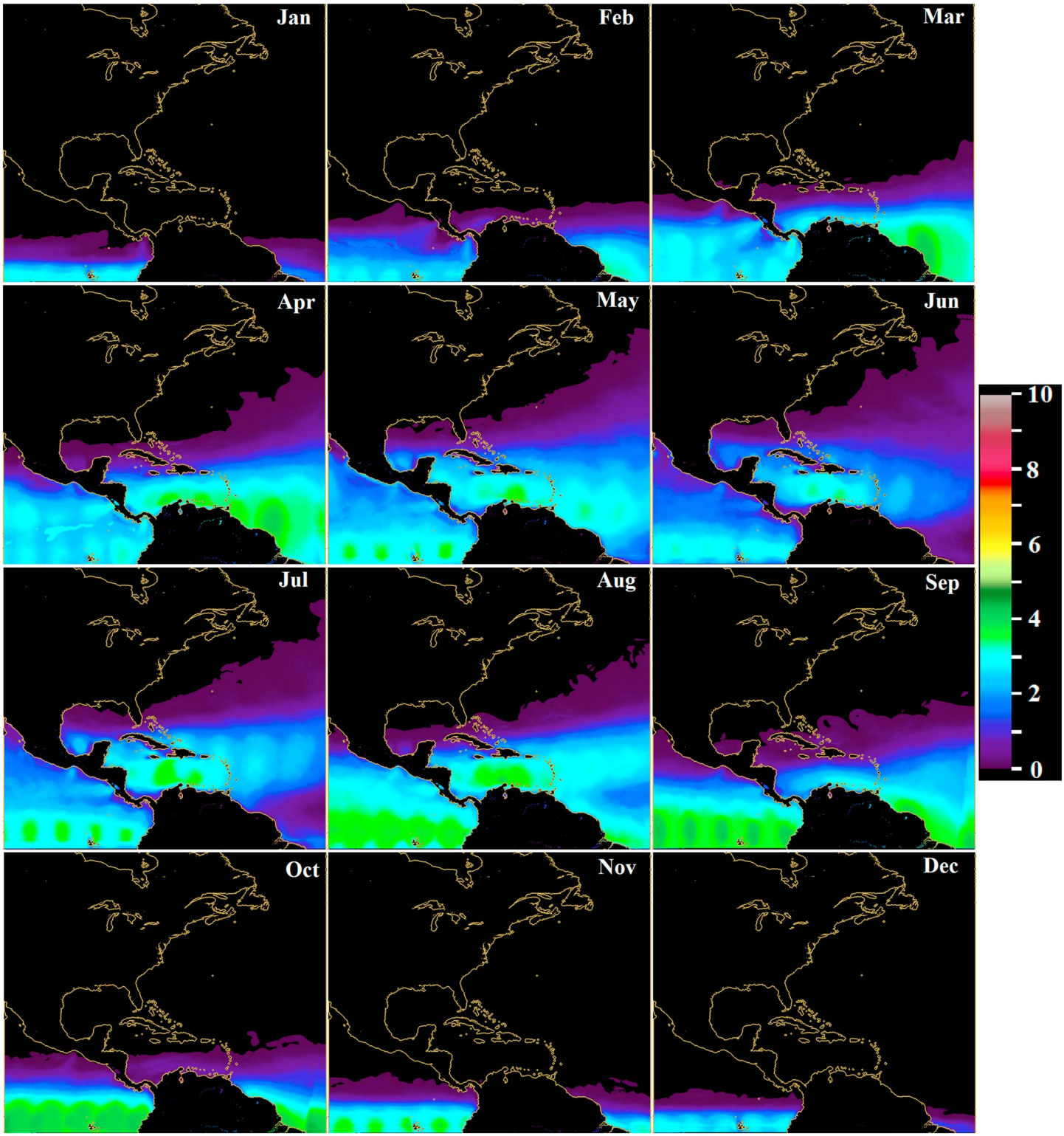


**Figure 4.** Mean number of Sun-glint-affected hourly observations within a day for each climatological month (2006–2011) from GEO-CAPE observation geometry for solar angle $\theta_o < 80°$. Here Sun glint is defined as the "high-glint" threshold used as the NASA standard quality control flag in composing global ocean color data products, namely, $L_{gn} \geq 0.005\ sr^{-1}$. Pixels associated with $L_{gn} \geq 0.005\ sr^{-1}$ are considered as low quality and not used in global composites. The asymmetric patterns across longitudes in May, June, and July are mainly due to changes in wind speeds, while some periodic circular patterns (e.g., in September) are due to changes in Sun angle from the hourly measurements. Statistics for the predefined subregions are presented in Table 3.

**Table 3.** Mean Number of Sun-Glint-Affected ($L_{gn} > 0.005$ sr$^{-1}$) Hourly Observations Within a Day for Each Climatological Month Between 2006 and 1010, Based on GEO-CAPE Viewing Geometry and GOES-Provided Winds[a]

| | E_Atlantic | Amazon | Caribbean | E_N_America | G_Lakes | SW_N_America | CA_Upwelling | GoM | WFS |
|---|---|---|---|---|---|---|---|---|---|
| Jan | 0 (0) | 0.8 (0.2) | 0 (0) | 0 (0) | 0 (0) | 0.3 (0) | 0.1 (0.1) | 0 (0) | 0 (0) |
| Feb | 0.8 (0.3) | 2.8 (1.1) | 0.3 (0.2) | 0 (0) | 0 (0) | 0.9 (0.4) | 0 (0) | 0.3 (0.2) | 0 (0) |
| Mar | 1.7 (0.8) | 3.5 (1.6) | 1.3 (0.6) | 0 (0) | 0 (0) | 1.7 (0.8) | 0 (0) | 1.1 (0.5) | 0 (0) |
| Apr | 1.6 (0.8) | 3.3 (1.5) | 2.4 (1.1) | 0.2 (0.1) | 0 (0) | 2.1 (1) | 0 (0.1) | 1.6 (0.8) | 0 (0) |
| May | 1.4 (0.1) | 2 (0.3) | 2.7 (0.2) | 1 (0.1) | 0.2 (0.2) | 2.1 (0.2) | 0 (0) | 1.7 (0.1) | 0.3 (0.2) |
| Jun | 0.9 (0.1) | 0.4 (0.1) | 2.3 (0.1) | 1 (0.2) | 0.2 (0.1) | 1.6 (0.1) | 0 (0) | 1.1 (0.1) | 0.4 (0.1) |
| Jul | 1.2 (0.1) | 0.9 (0.1) | 2.7 (0.2) | 1 (0.1) | 0.1 (0.1) | 2 (0.1) | 0 (0) | 1.5 (0.2) | 0.2 (0.1) |
| Aug | 1.7 (0.4) | 3 (0.6) | 2.7 (0.5) | 0.3 (0) | 0 (0) | 2.7 (0.4) | 0 (0) | 2.1 (0.4) | 0 (0) |
| Sep | 1.5 (0.5) | 3.5 (1.2) | 1.6 (0.6) | 0.1 (0.1) | 0 (0) | 2.1 (0.7) | 0 (0) | 1.2 (0.4) | 0 (0) |
| Oct | 0.7 (0.4) | 2.8 (1.4) | 0.3 (0.2) | 0 (0) | 0 (0) | 1.4 (0.7) | 0.4 (0.4) | 0.4 (0.2) | 0 (0) |
| Nov | 0 (0) | 1.4 (0.1) | 0 (0) | 0 (0) | 0 (0) | 0.9 (0.1) | 1.5 (1.1) | 0.1 (0) | 0 (0) |
| Dec | 0 (0) | 0.5 (0.3) | 0 (0) | 0 (0) | 0 (0) | 0.5 (0.3) | 0.2 (0.3) | 0 (0) | 0 (0) |
| Mean | 1 (0.3) | 2.1 (0.7) | 1.3 (0.3) | 0.3 (0.1) | 0.1 (0) | 1.5 (0.4) | 0.2 (0.2) | 0.9 (0.2) | 0.1 (0) |

[a]Numbers in the parentheses are standard deviations. Spatial distributions are presented in Figure 4.

(and also positive offsets) when cloud-free probability is low (<0.4 for June and <0.2 for December; Figure 8). Figure 7 shows that these regions are mainly around the Intertropical Convergence Zone (ITCZ), where high temperature causes abundant evaporation and convection, leading to cloudy weather for this region throughout the year [*Haug et al*., 2001]. Consequently, cloud morphology may be different from other regions, leading to different cloud detection results from GOES and Aqua observations. Nevertheless, the overall results indicate that they are generally comparable between GOES and MODIS/Aqua for both spatial and temporal patterns.

The differences due to resolution changes are also observed in MODIS data alone between 1 km and 250 m resolutions. As shown in Figure 9, for the entire GoM (18–31°N, 98–79°W), MODIS 1 km data show higher cloud cover than 250 m data for both Terra and Aqua, with the difference in $P_{cf}$ often exceeding 20% in summer months. This observation is consistent with those observed between GOES 4 km and MODIS 1 km data; i.e., finer resolution leads to less cloud cover and higher cloud-free probability for a given location. Furthermore, the differences in cloud cover between Terra (10:30 local overpass) and Aqua (13:30 local overpass) generally concur with the GOES-based observations of diurnal differences in cloud cover.

## 5. Discussion

### 5.1. Uncertainties in GOES-Based and MODIS-Based Cloud Statistics

The GOES cloud mask is derived from a probabilistic approach which allows for the generation of an uncertainty estimate. As shown in *Heidinger et al*. [2012], the uncertainties of the cloud detection over daytime ocean are generally less than 5%. Independent comparisons against the cloud layer product derived from the Cloud-Aerosol Lidar with Orthogonal Polarization (CALIOP) onboard the NASA Cloud-Aerosol Lidar and Infrared Pathfinder Satellite Observations (CALIPSO) satellite confirm that the uncertainties for daytime ocean are less than 10%. Uncertainties grow in regions of oceanic glint, but these would not impact the performance of GEO-CAPE.

Does the cloud cover over the same location change significantly from year to year? If so, the cloud statistics would be meaningless for planning the GEO-CAPE mission. This hypothesis can be rejected by the following two reasons. First, global weather is controlled primarily by major atmospheric and oceanic circulation. Although the strengths of these circulation patterns change between different years (especially during El Niño /La Niña years), the overall patterns of the Earth's weather are relatively stable during a certain period [*Barry and Chorley*, 2009]. For example, the equatorial Pacific Ocean and Atlantic Ocean are located within the ITCZ, where cloudy weather prevails throughout the year [*Haug et al*., 2001]. Likewise, the rapid seasonal changes of the cloud coverage in the southwestern coast of North America are likely attributed to the North American monsoon, where the evidently higher precipitation in boreal summer months is due to a high pressure called the subtropical ridge [*Adams and Comrie*, 1997]. Similarly, the seasonality of cloud cover in the other major oceans should also be associated with certain circulation patterns.

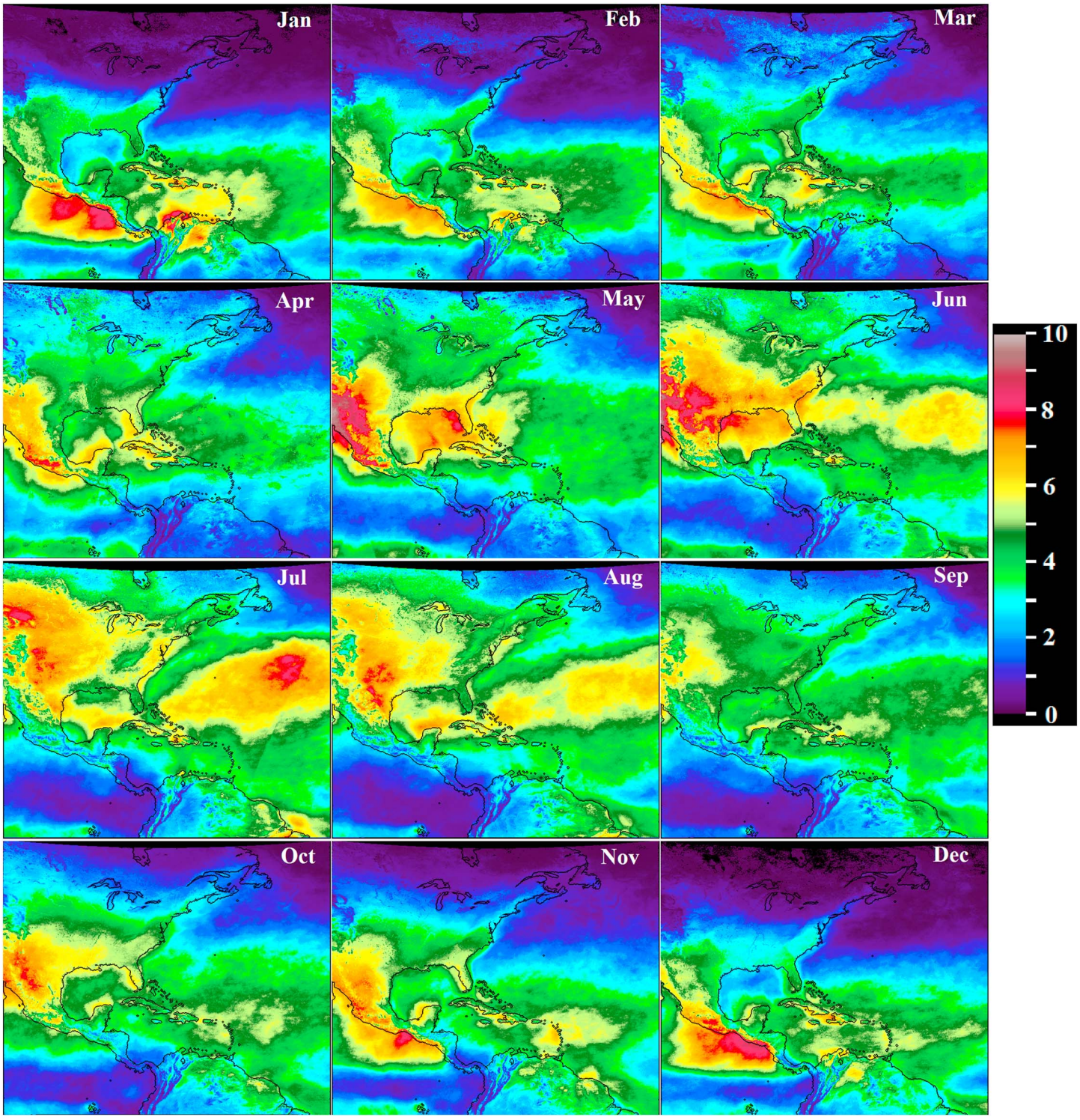


**Figure 5.** Mean number of simultaneous cloud-free and glint-free hourly observations per day ($N_{cf}$). This is the same as in Figure 2 but excluding observations with $L_{gn} \geq 0.005$ sr$^{-1}$ in Figure 4.

Second, as demonstrated in the example shown in Figure 10, the overall patterns for $N_{cf}$ are similar between the six observed years from 2006 to 2011 in January, with relatively high values in the southwestern coast of North America, the Caribbean Sea, and a large portion of the western Atlantic and lower values over the high-latitude oceans and equatorial regions. The comparisons for other months also show similar agreements of $N_{cf}$ between

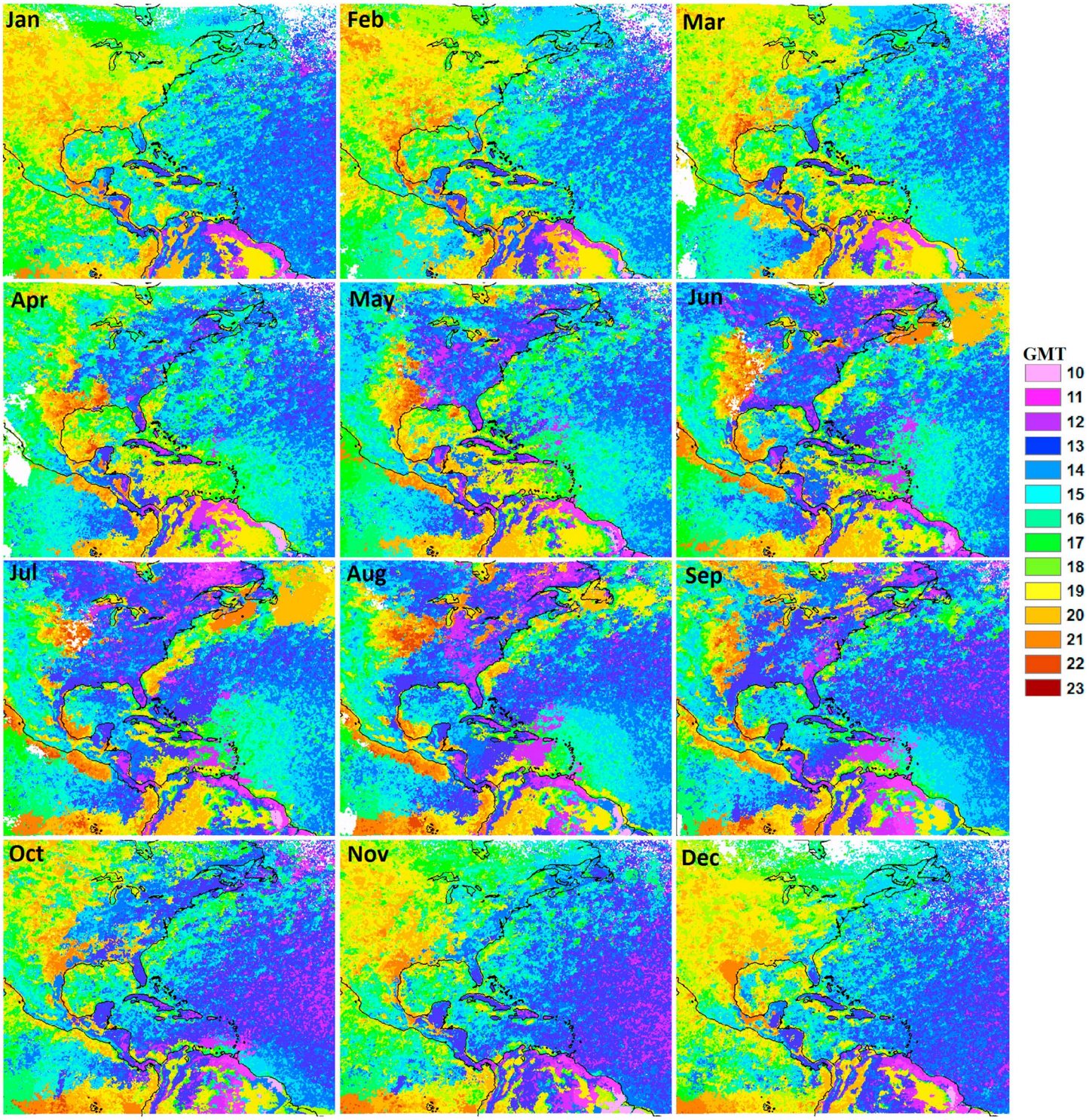


**Figure 6.** GMT hour corresponding to maximal cloud-free and glint-free probabilities during a day for each climatological month (2006–2011) for solar angle $\theta_o < 80°$. Glint free is defined as $L_{gn} < 0.005\ sr^{-1}$. Statistics for the predefined subregions are presented in Table 4.

different years. The similarity of cloud cover between different years can also be revealed through the relatively small standard derivations (STDs) in the climatological monthly $N_{cf}$ or $P_{cf}$ for the predefined regions (Tables 1 and 3), with STDs generally less than half (and often <10%) of the corresponding mean values. Moreover, the Multivariate El Niño–Southern Oscillation (ENSO) Index showed little variability in the 2000s when it was

**Table 4.** GMT Hour Corresponding to Maximal Cloud-Free and Glint-Free Probability During a Day for Each Climatological Month (2006–2010) for Solar Angle $\theta_o < 80°$[a]

| | E_Atlantic | Amazon | Caribbean | E_N_America | G_Lakes | SW_N_America | CA_Upwelling | GoM | WFS |
|---|---|---|---|---|---|---|---|---|---|
| Jan | 14 | 14 | 16 | 16 | 19 | 20 | 20 | 21 | 18 |
| Feb | 14 | 14 | 20 | 16 | 18 | 20 | 20 | 20 | 17 |
| Mar | 14 | 15 | 20 | 15 | 19 | 16 | 21 | 20 | 16 |
| Apr | 14 | 14 | 20 | 14 | 19 | 15 | 21 | 20 | 18 |
| May | 14 | 14 | 20 | 15 | 19 | 15 | 22 | 20 | 20 |
| Jun | 14 | 14 | 20 | 22 | 20 | 16 | 22 | 15 | 19 |
| Jul | 14 | 14 | 14 | 22 | 20 | 16 | 22 | 15 | 19 |
| Aug | 14 | 14 | 13 | 21 | 20 | 15 | 22 | 15 | 19 |
| Sep | 13 | 15 | 13 | 15 | 20 | 15 | 21 | 15 | 17 |
| Oct | 13 | 14 | 13 | 15 | 19 | 20 | 20 | 20 | 20 |
| Nov | 13 | 14 | 13 | 15 | 17 | 19 | 19 | 20 | 20 |
| Dec | 14 | 14 | 15 | 15 | 19 | 20 | 20 | 20 | 20 |

[a]For each region and month, the number shown in the table represents the mode of the histogram of the optimal hours (for cloud-free probability) from all pixels. Glint free is defined as $L_{gn} < 0.005\ sr^{-1}$. Spatial distributions are presented in Figure 6.

compared with previous decades (http://www.esrl.noaa.gov/psd/enso/mei/), indicating that the observed period of 2006–2011 would represent the mean cloud conditions during calm ENSO conditions. Thus, the results presented in this study could be used to represent the mean cloud cover conditions in the Intra-Americas Sea. In contrast, data statistics for strong El Nino years (e.g., 1998 and 2016) may not be used here as the weather conditions during these years may be significantly different from those of normal years.

Similar to GOES cloud cover data product, the MODIS MOD35 cloud mask product has also been evaluated and validated extensively through the use of measurements from both ground- and satellite-based instruments. Agreement in cloud detection between the collection 5 MOD35 and active remotely sensed cloud

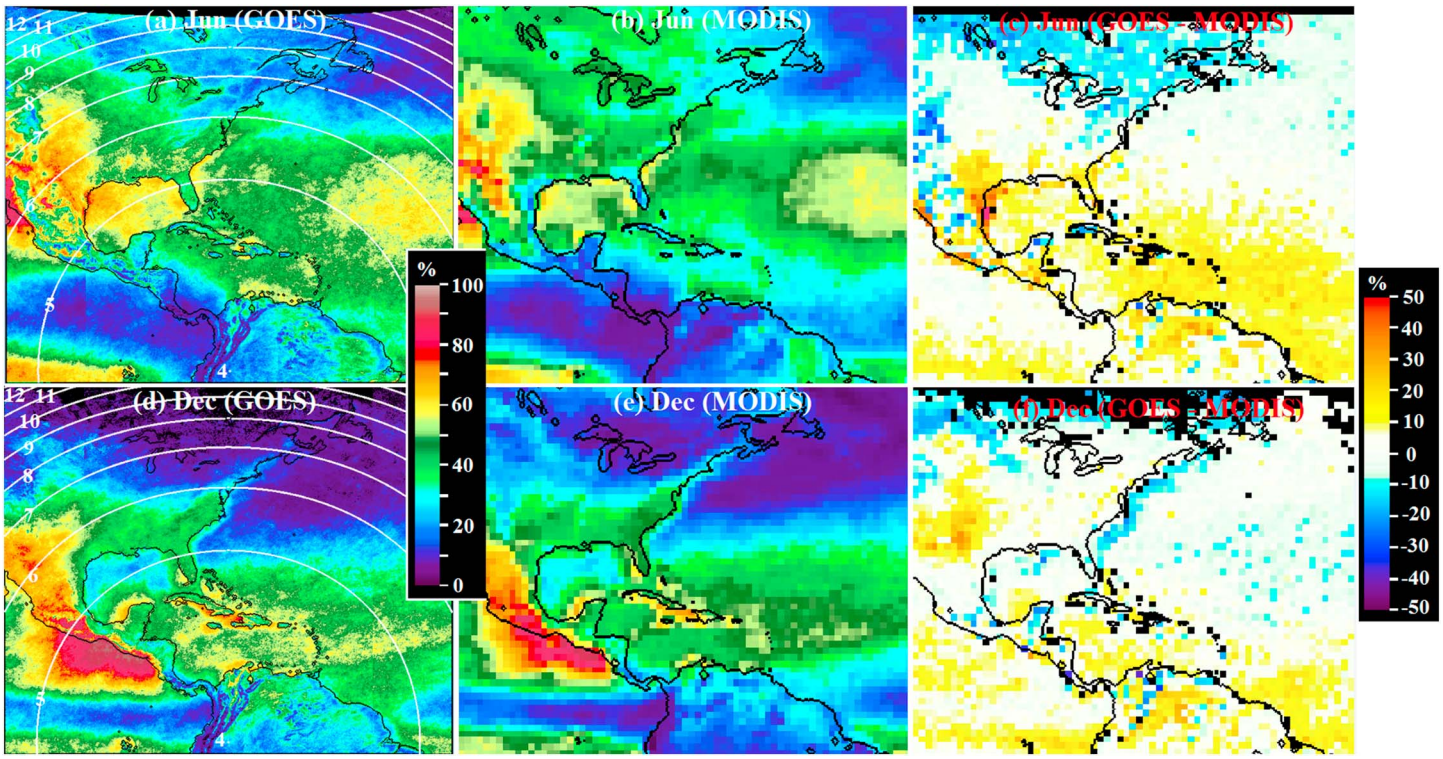


**Figure 7.** Comparison between (a and d) GOES and (b and e) MODIS/Aqua cloud-free probability estimates and (c and f) the corresponding differences (GOES − MODIS) for June and December 2006–2010. MODIS results are obtained from the standard 1 km MOD35 cloud mask products and binned to 1° resolution, with equatorial crossing time around 13:30 local time, while GOES results are from 4 km nadir resolution observations at 13:15 local time. The contours of GOES original pixel sizes are annotated in Figures 7a and 7d.

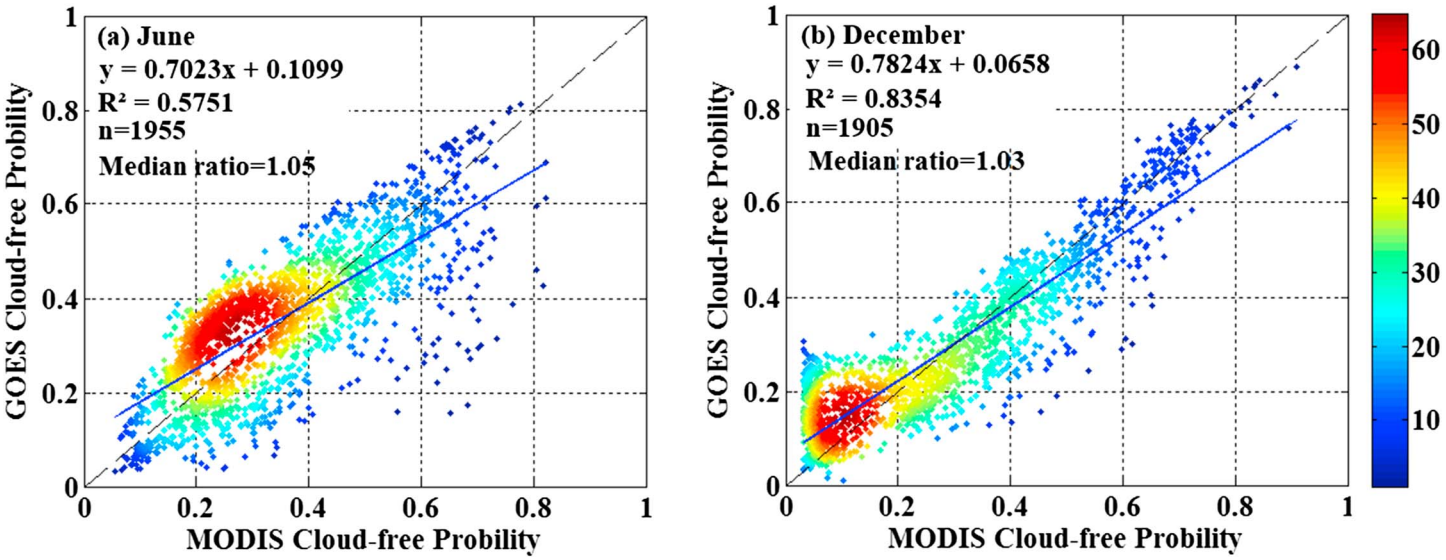


**Figure 8.** Same as in Figure 7, but data are provided in scatterplots. The black solid lines are the 1:1 lines, and the red dashed lines are the linear fitting lines. Note that these statistics were computed from ocean pixels only, with land pixels from Figure 7 removed.

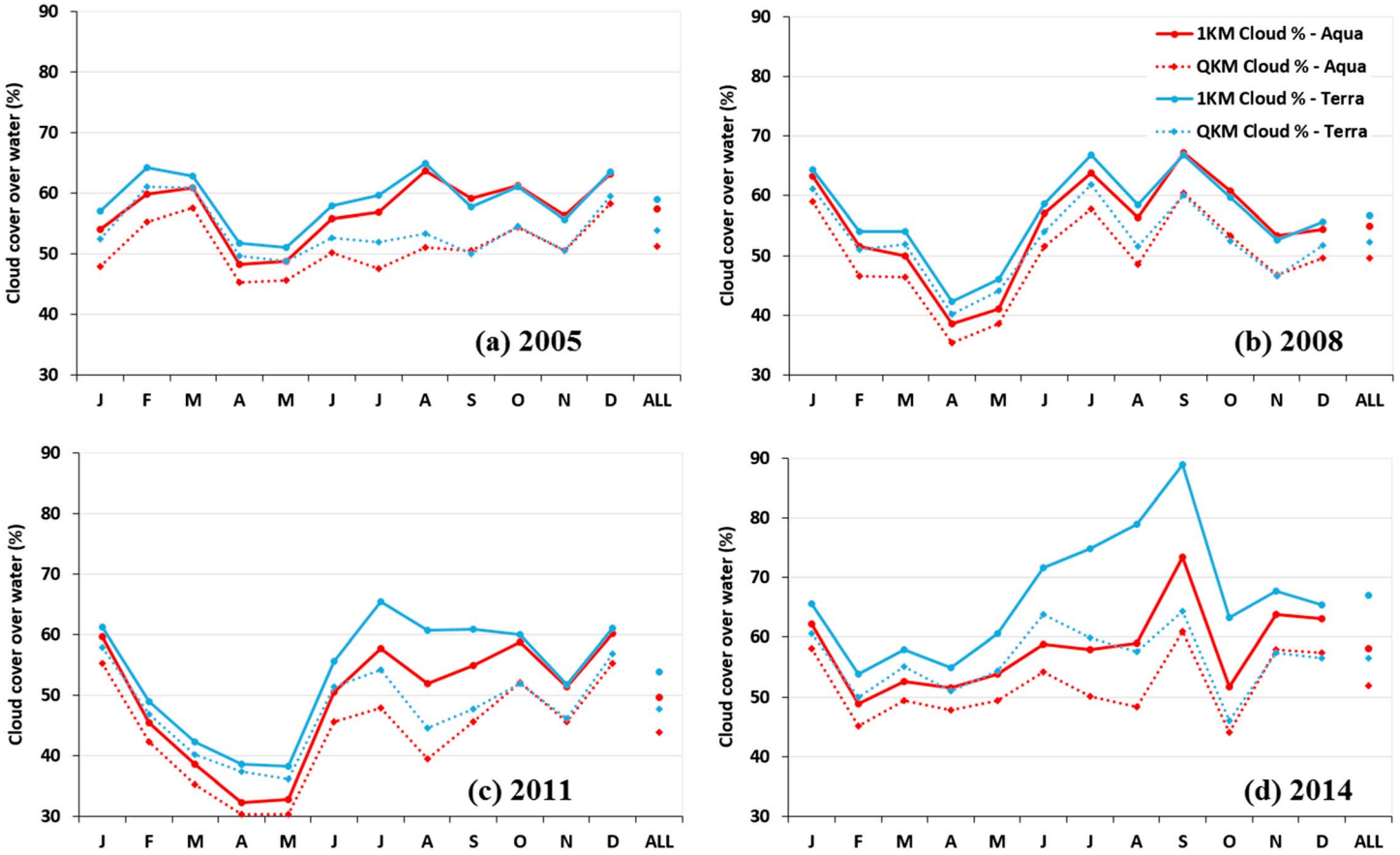


**Figure 9.** Comparison between MODIS percent cloud cover over the Gulf of Mexico (18°N–31°N, 98°W–79°W) using 1 km and QKM MOD35 cloud mask products for both MODIS/Aqua and MODIS/Terra, where the 1 km and QKM cloud coverage data were not independent. The annual mean cloud cover is also shown in every panel (right hand of horizontal axis, with a tick name of "ALL").

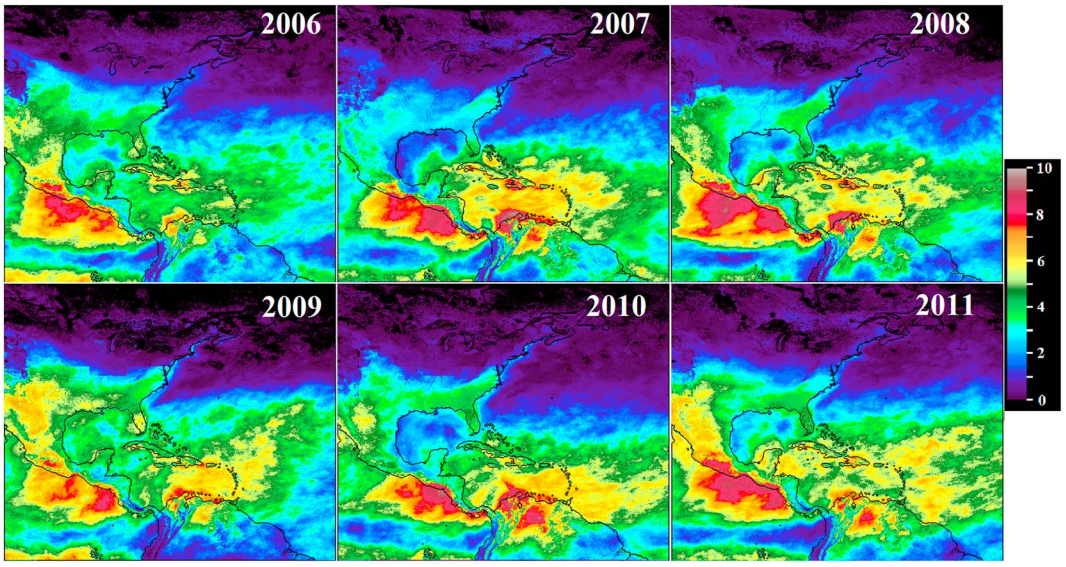


**Figure 10.** Comparison of $N_{cf}$ in January of 2006–2011 from GOES observations. While small differences are observed, the overall distribution patterns are similar in different years. Same observation is obtained for all other months.

ground-based lidar and radar in the Central U.S. was about 85% [*Ackerman et al.*, 2008]. It was also established that about 90% of nonpolar disagreements between MOD35 and ground-based lidar were for clouds with optical depths $<$0.4. More recent and comprehensive comparisons of collection 6 MOD35 to CALIOP satellite lidar indicate monthly global agreements (hit rates) in cloud detection of about 88% but higher values in nonpolar regions (about 90%) (Richard Frey 2016, personal communication) [*Holz et al.*, 2008]. Note that these numbers represent the uncertainties from individual points instead of systematic bias, therefore will not likely impact the analysis of spatial patterns and temporal changes used in this study.

### 5.2. Implications for GEO-CAPE Measurement Strategy

The results presented here have significant implications for developing an optimal GEO-CAPE measurement strategy to maximize its capacity to take high-frequency measurements while avoiding cloud cover and Sun glint. Indeed, the GOES-East satellite data used in this study cover a large portion of the planned FOV for GEO-CAPE, and the Sun-glint calculations are based on planned GEO-CAPE satellite location at 94°W. The significant resources required to build and launch a GEO-CAPE ocean color sensor to measure *every* region within the 67° sensor view angle at hourly frequency on a routine monitoring mode are not available [*Fishman et al.*, 2012]; thus, where, when, and how often to scan a certain region should be determined. Although, in practice, the local oceanography (e.g., bloom season) and science requirements also need to be considered, the results here can be used to determine the best time windows to avoid cloud and Sun glint for different regions. For example, the optimal time to observe the southern coast of North America is 19–20 (GMT hour) from November to February and 15–16 (GMT hour) from March to April, which ironically occur before and after the MODIS-Aqua overpass (approximately 1700 to 1830). Rules for other regions could also be easily determined using the tables and figures shown in this study. The cloud cover information throughout the day can be applied in GEO-CAPE scheduling studies to determine the temporal frequency that any given region can be observed during any given month for any notional instrument concept. Furthermore, these data can be applied to develop and test an autonomous scheduling system that optimizes the spatial coverage and number of hourly observations. The cloud cover information throughout the day can be applied in GEO-CAPE scheduling studies to determine the temporal frequency that any given region can be observed during any given month for any notional instrument concept. Preliminary scheduling studies [*Frank et al.*, 2016] for two instrument concepts clearly demonstrated how clouds reduce the number of viewable scenes, reduce competition for instrument time, and thus allow slower instruments to become more favorable in temporal metrics. Furthermore, these or similar data can be applied to develop and test an autonomous scheduling system that optimizes the spatial

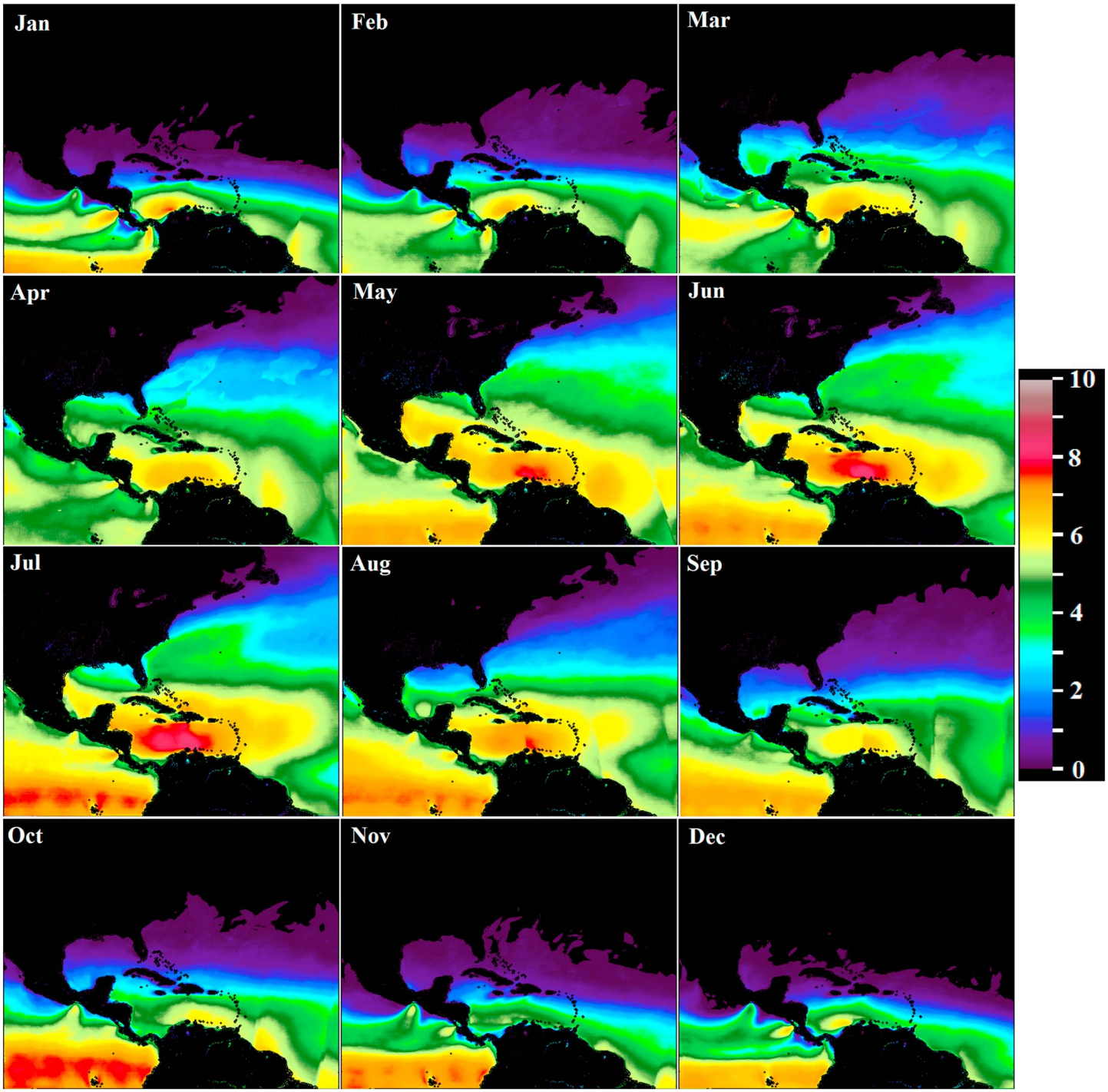


**Figure 11.** Number of hourly observations during a day (2006–2010) with Sun-glint reflectance ($L_{gn}$) $>10^{-5}$ $sr^{-1}$. Under such Sun-glint influence, surface oil slicks can always be observed due to surface wave damping [*Sun and Hu*, 2016].

coverage and number of hourly observations [*Cappelaere et al*., 2015]. In addition, low-Earth orbit missions such as PACE or JPSS can utilize these results to optimize spatial resolution for more cloud-free observations whenever the trade space allows.

Note that the GOES-derived cloud statistics are based on 4 km resolution measurements, and cloud cover has been shown to be sensitive to spatial resolution. Although the average differences between 4 km and 1 km and between 1 km and 250 m are not large (about 10%), in certain months or regions the difference between

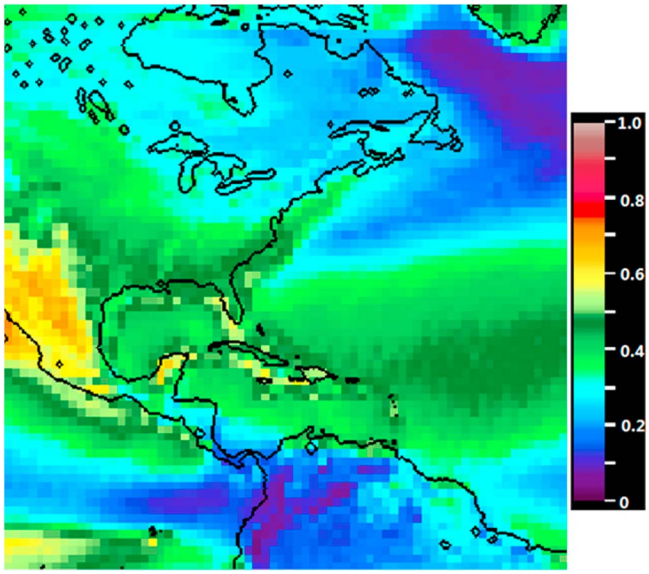


**Figure 12.** Mean number of cloud-free observations during a day based on MODIS observations between 2006 and 2011. Note that the maximum number is <1.0 from the polar-orbiting sensor. The figure serves as a reference to compare with those obtained from hourly geostationary observations by GOES (Figure 1).

4 km and 1 km and between 1 km and 250 m could reach 30% or higher. For example, during summer months over the GoM the 250 m MODIS data show 20% less cloud cover than 1 km MODIS data (Figure 9). Although these differences are unlikely to change the overall spatial/temporal patterns of GOES-based cloud statistics, they do support finer spatial resolutions in order to minimize cloud cover effects. In this regard, the 375 m nadir resolution of GEO-CAPE is a reasonable choice to increase cloud-free probability over the standard 1 km ocean color observations, and this is in addition to meeting the science requirements to address small-scale oceanographic processes. The increased cloud-free coverage is mostly near small cloud patches, where the pixels are contaminated by stray light and thus deemed as being low quality [*Feng and Hu*, 2016a]. However, with continuous progress in algorithm improvement some of these cloud-adjacent pixels may be "recovered" to meet the science requirement [e.g., *Feng and Hu*, 2016a].

Although for ocean color measurements Sun glint is often avoided (e.g., SeaWiFS is tilted to avoid Sun glint), the presence of Sun glint can facilitate observing certain ocean surface features such as internal waves [*Jackson*, 2007] and oil slicks [*Adamo et al.*, 2009; *Hu et al.*, 2009]. A recent study by *Sun and Hu* [2016] showed that when $L_{gn}$ is $>10^{-5}$ sr$^{-1}$, even the thinnest surface oil films from natural seeps can always be detected by MODIS or VIIRS. The number of hourly observations during a day (2006–2011) with $L_{gn} > 10^{-5}$ sr$^{-1}$ for GEO-CAPE observing geometry ($N_t$) are shown in Figure 11. This is also informative for GEO-CAPE measurement planning, as one of the objectives of GEO-CAPE is to monitor oil spills [*Fishman et al.*, 2012]. Generally, higher $N_t$ values can be identified in the warm months than in cold months, especially in the tropical and subtropical oceans of the Caribbean, GoM, and the equatorial regions. These results can be used to determine the best months to map the nature oil slicks using future GEO-CAPE observations. For example, May to July appear to be the optimal period for hourly observations in the GoM, as $N_t$ in these months is >4.

Finally, although it is intuitive that $N_{cf}$ from polar orbiters is always <1.0 except for polar regions, it would be interesting to have a visual inspection in reference against those from GOES observations. Figure 12 presents such an example, where distributions of $N_{cf}$ from MODIS/Aqua measurements between 2006 and 2011 are demonstrated. For most locations $N_{cf}$ is <0.5. In contrast, from GOES observations most locations showed $N_{cf} > 2.0$, suggesting a significant improvement in cloud-free measurements from geostationary platforms.

## 6. Conclusions

Using GOES hourly observations at 4 km nadir resolution from 2006 to 2011 and measurement geometry of GEO-CAPE, this study provides the first statistical results of cloud cover and Sun glint over the Intra-Americas Sea. The climatological numbers of cloud-free and glint-free hourly observations within a day (solar zenith angle <80°) are estimated and presented in both graphical and tabular forms for each of the predefined subregions. Significant spatial and seasonal variabilities in both cloud and Sun glint patterns are observed. The comparison of cloud statistics derived from several years of MODIS 1 km and 250 m observations over the GoM also shows improved cloud-free probability with finer resolution. Given the limited resources anticipated for the GEO-CAPE mission, the findings here support a geostationary sensor with subkilometer resolution and

may be used to help plan the optimal observation time window for a certain region. We hope to incorporate these findings in the future implementation of the GEO-CAPE measurement plan.

## Notations

| | |
|---|---|
| GOES | Geostationary Operational Environmental Satellite system (1974 to present) |
| CZCS | Coastal Zone Color Scanner (1978–1986) |
| SeaWiFS | Sea-viewing Wide Field-of-view Sensor (1997–2010) |
| MERIS | Medium Resolution Imaging Spectrometer (2002–2012) |
| MODIS | Moderate Resolution Spectroradiometer (1999 on Terra and 2002 on Aqua) |
| GOCI | Geostationary Ocean Color Imager (2010 to present) |
| VIIRS | Visible Infrared Imaging Radiometer Suite (2011 to present) |
| GEO-CAPE | Geostationary Coastal and Air Pollution Events |
| PACE | Plankton, Aerosol, Cloud, ocean Ecosystem |
| OLCI | Ocean and Land Colour Instrument |
| NASA | U.S. National Aeronautics and Space Administration |
| GIOVANNI | Geospatial Interactive Online Visualization And aNalysis Infrastructure |
| CFSR | Climate Forecast System Reanalysis |
| Chl *a* | Chlorophyll *a* concentration ($mg\,m^{-3}$) |
| nFLH | Normalized Florescence Line Height ($mw^{-2}\,cm^{-2}\,\mu m^{-1}\,sr^{-1}$) |
| $L_{gn}$ | Normalized Sun-glint reflectance ($sr^{-1}$) |
| $\theta_o$ | Solar zenith angle |
| FOV | Field of view |
| $N_{cf}$ | Number of cloud-free hourly observations per day |
| $N_{sg}$ | Number of Sun-glint-affected hourly observations per day |
| $N_{cg}$ | Number of cloud-free and glint-free hourly observations per day |
| $N_t$ | Number of hourly observations per day with $L_{gn} > 10^{-5}\,sr^{-1}$ |
| $P_{cf}$ | Integrated daily cloud-free probability |
| $T_{max}$ | Time of a day (or GMT hour in specific) that has the maximal cloud-free and glint-free probability |
| $C_f$ | Cloud fraction |
| DPVOs | Mean daily percentage of valid observations |
| GoM | Gulf of Mexico |
| WFS | West Florida Shelf |
| ITCZ | Intertropical Convergence Zone |
| STD | Standard derivation |

**Acknowledgments**

This work was supported by the NASA Ocean Biology and Biogeochemistry program and particularly through a grant to support NASA's GEO-CAPE mission design. The views, opinions, and findings contained in this report are those of the author(s) and should not be construed as an official National Oceanic and Atmospheric Administration or U.S. Government position, policy, or decision. The manuscript received extensive comments and suggestions from four reviewers, whose effort to help improve the manuscript is greatly appreciated. The GOES cloud mask data were provided by the NOAA, from their website at http://www.ospo.noaa.gov/Products/atmosphere/clavr/index.html. MODIS cloud fraction data were obtained from the NASA's Giovanni website at http://giovanni.gsfc.nasa.gov/giovanni/. MODIS level 1A data were obtained from the NASA's OceanColor Web at http://oceancolor.gsfc.nasa.gov/cms/.

## References

Acker, J. G., and G. Leptoukh (2007), Online analysis enhances use of NASA Earth science data, *Eos Trans. AGU*, *88*(2), 14–17.

Ackerman, S., K. I. Strabala, W. P. Menzel, R. A. Frey, C. C. Moeller, and L. E. Gumley (1998), Discriminating clear sky from clouds with MODIS, *J. Geophys. Res.*, *103*(D24), 32,141–32,157, doi:10.1029/1998JD200032.

Ackerman, S., R. Holz, R. Frey, E. Eloranta, B. Maddux, and M. McGill (2008), Cloud detection with MODIS. Part II: Validation, *J. Atmos. Oceanic Technol.*, *25*(7), 1073–1086.

Adamo, M., G. De Carolis, V. De Pasquale, and G. Pasquariello (2009), Detection and tracking of oil slicks on Sun-glittered visible and near infrared satellite imagery, *Int. J. Remote Sens.*, *30*(24), 6403–6427.

Adams, D. K., and A. C. Comrie (1997), The North American monsoon, *Bull. Am. Meteorol. Soc.*, *78*(10), 2197–2213.

Aurin, D., A. Mannino, and B. Franz (2013), Spatially resolving ocean color and sediment dispersion in river plumes, coastal systems, and continental shelf waters, *Remote Sens. Environ.*, *137*, 212–225.

Barnes, B. B., and C. Hu (2015), Cross-sensor continuity of satellite-derived water clarity in the Gulf of Mexico: Insights into temporal aliasing and implications for long-term water clarity assessment, *Geosci. Remote Sens. IEEE Trans.*, *53*(4), 1761–1772.

Barry, R. G., and R. J. Chorley (2009), *Atmosphere, Weather and Climate*, 9th ed., Routledge, Taylor and Francis, London and New York.

Cappelaere, P., S. Frye, K. Moe, D. Mandl, J. LeMoigne, T. Flatley, and A. Geist (2015), Strategies GeoCape intelligent observation studies@GSFC, paper presented at GEO-CAPE Workshop, Research Triangle Park, NC., http://ntrs.nasa.gov/search.jsp?N=0&Ntk=All&Ntt=GSFC-E-DAA-TN26450&Ntx=mode%20matchall. Date accessed: 05 Oct. 2016. See also: http://geocape.herokuapp.com.

Choi, J.-K., Y. J. Park, J. H. Ahn, H.-S. Lim, J. Eom, and J.-H. Ryu (2012), GOCI, the world's first geostationary ocean color observation satellite, for the monitoring of temporal variability in coastal water turbidity, *J. Geophys. Res.*, *117*, C09004, doi:10.1029/2012JC008046.

Cox, C., and W. Munk (1954), Measurement of the roughness of the sea surface from photographs of the Sun's glitter, *J. Opt. Sci. Am.*, *44*(11), 838–850.
Feng, L., and C. Hu (2016a), Cloud adjacency effects on top-of-atmosphere radiance and ocean color data products: A statistical assessment, *Remote Sens. Environ.*, *174*, 301–313.
Feng, L., and C. Hu (2016b), Comparison of valid ocean observations between MODIS Terra and Aqua over the global oceans, *Geosci. Remote Sens. IEEE Trans.*, *54*, 1575–1585.
Fishman, J., L. Iraci, J. Al-Saadi, K. Chance, F. Chavez, M. Chin, P. Coble, C. Davis, P. DiGiacomo, and D. Edwards (2012), The United States' next generation of atmospheric composition and coastal ecosystem measurements: NASA's Geostationary Coastal and Air Pollution Events (GEO-CAPE) mission, *Bull. Am. Meteorol. Soc.*, *93*(10), 1547–1566.
Frank, J., M. Do, and T. Tran (2016), Scheduling ocean color observations for a GEO-stationary satellite, paper presented at Twenty-Sixth International Conference on Automated Planning and Scheduling, London. [Available at http://www.aaai.org/ocs/index.php/ICAPS/ICAPS16/paper/view/13072.]
Gordon, H. R. (1997), Atmospheric correction of ocean color imagery in the Earth Observing System era, *J. Geophys. Res.*, *102*(D14), 17,081–17,106, doi:10.1029/96JD02443.
Haug, G. H., K. A. Hughen, D. M. Sigman, L. C. Peterson, and U. Röhl (2001), Southward migration of the Intertropical Convergence Zone through the Holocene, *Science*, *293*(5533), 1304–1308.
He, X., Y. Bai, D. Pan, N. Huang, X. Dong, J. Chen, C.-T. A. Chen, and Q. Cui (2013), Using geostationary satellite ocean color data to map the diurnal dynamics of suspended particulate matter in coastal waters, *Remote Sens. Environ.*, *133*, 225–239.
Heidinger, A. K., A. T. Evan, M. J. Foster, and A. Walther (2012), A naive Bayesian cloud-detection scheme derived from CALIPSO and applied within PATMOS-x, *J. Appl. Meteorol. Climatol.*, *51*(6), 1129–1144.
Heidinger, A. K., M. J. Foster, A. Walther, and X. Zhao (2014), The pathfinder atmospheres-extended AVHRR climate dataset, *Bull. Am. Meteorol. Soc.*, *95*(6), 909–922.
Holz, R., S. Ackerman, F. Nagle, R. Frey, S. Dutcher, R. Kuehn, M. Vaughan, and B. Baum (2008), Global Moderate Resolution Imaging Spectroradiometer (MODIS) cloud detection and height evaluation using CALIOP, *J. Geophys. Res.*, *113*, D00A19, doi:10.1029/2008JD009837.
Hu, C., X. Li, W. Pichel, and F. Muller-Karger (2009), Detection of natural oil slicks in the NW Gulf of Mexico using MODIS imagery, *Geophys. Res. Lett.*, *36*, L01604, doi:10.1029/2009GL039655.
Huang, H.-L., L. E. Gumley, K. Strabala, J. Li, E. Weisz, T. Rink, K. C. Baggett, J. E. Davies, W. L. Smith, and J. C. Dodge (2004), International MODIS and AIRS Processing Package (IMAPP): A direct broadcast software package for the NASA Earth Observing System, *Bull. Am. Meteorol. Soc.*, *85*(2), 159–161.
Jackson, C. (2007), Internal wave detection using the Moderate Resolution Imaging Spectroradiometer (MODIS), *J. Geophys. Res.*, *112*, C11012, doi:10.1029/2007JC004220.
King, M. D., S. Platnick, W. P. Menzel, S. A. Ackerman, and P. A. Hubanks (2013), Spatial and temporal distribution of clouds observed by MODIS onboard the Terra and Aqua satellites, *IEEE Trans. Geosci. Remote Sens.*, *51*, 3826–3852.
Kirk, J. T. (1994), *Light and Photosynthesis in Aquatic Ecosystems*, Cambridge Univ. Press, Cambrige and New York.
Lombardi, M. A., and D. W. Hanson (2005), The GOES time code service, 1974–2004: A retrospective, *J. Res. Nat. Inst. Stand. Tech.*, *110*(2), 79.
Lou, X., and C. Hu (2014), Diurnal changes of a harmful algal bloom in the East China Sea: Observations from GOCI, *Remote Sens. Environ.*, *140*, 562–572.
Maritorena, S., O. H. F. d'Andon, A. Mangin, and D. A. Siegel (2010), Merged satellite ocean color data products using a bio-optical model: Characteristics, benefits and issues, *Remote Sens. Environ.*, *114*(8), 1791–1804.
McClain, C. R. (2009), A decade of satellite ocean color observations, *Annu. Rev. Mar. Sci.*, *1*, 19–42.
Meister, G., and C. R. McClain (2010), Point-spread function of the ocean color bands of the Moderate Resolution Imaging Spectroradiometer on Aqua, *Appl. Opt.*, *49*(32), 6276–6285.
NRC (2007), *Earth Science and Applications from Space: National Imperatives for the Next Decade and Beyond*, The National Academies Press, 400 pp.
Platnick, S., M. D. King, S. A. Ackerman, W. P. Menzel, B. A. Baum, J. C. Riédi, and R. A. Frey (2003), The MODIS cloud products: Algorithms and examples from Terra, *Geosci. Remote Sens. IEEE Trans.*, *41*(2), 459–473.
Richharia, M. (2014), *Mobile Satellite Communications (in Appendix)*, pp. 703–714, John Wiley, New York, doi:10.1002/9781118810170.app1.
Son, Y. B., J.-E. Min, and J.-H. Ryu (2012), Detecting massive green algae (*Ulva prolifera*) blooms in the Yellow Sea and East China Sea using Geostationary Ocean Color Imager (GOCI) data, *Ocean Sci. J.*, *47*(3), 359–375.
Sun, S., and C. Hu (2016), Sun glint requirement for the remote detection of surface oil films, *Geophys. Res. L ett.*, *43*, 309–316, doi:10.1002/2015GL066884.
Várnai, T., and A. Marshak (2014), Near-cloud aerosol properties from the 1 km resolution MODIS ocean product, *J. Geophys. Res. Atmos.*, *119*, 1546–1554, doi:10.1002/2013JD020633.
Várnai, T., and A. Marshak (2015), Effect of cloud fraction on near-cloud aerosol behavior in the MODIS atmospheric correction ocean color product, *Remote Sens.*, *7*(5), 5283–5299.
Wang, M., and S. W. Bailey (2001), Correction of Sun glint contamination on the SeaWiFS ocean and atmosphere products, *Appl. Opt.*, *40*(27), 4790–4798.
Zhang, H., and M. Wang (2010), Evaluation of Sun glint models using MODIS measurements, *J. Quant. Spectros. Radiat. Transfer*, *111*(3), 492–506.